Turkish Journal of
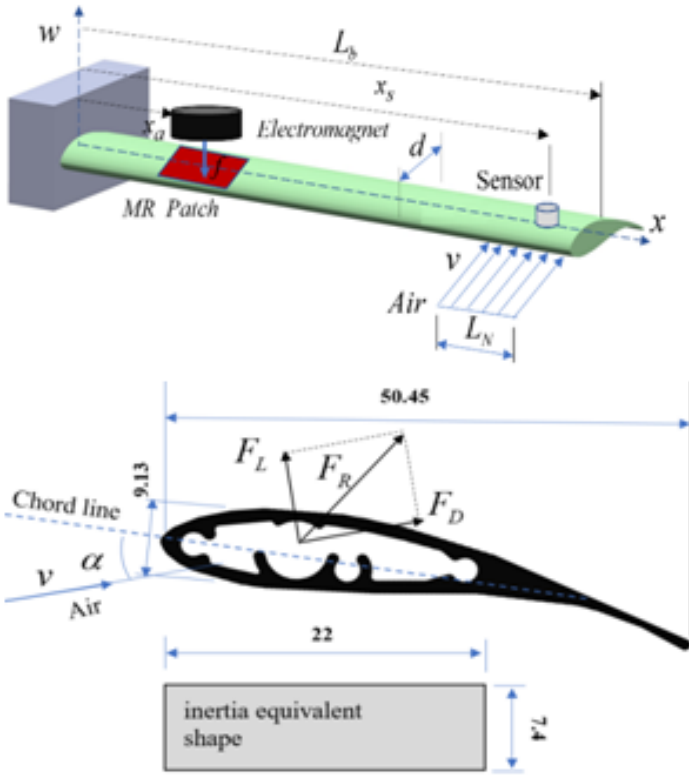
Electromechanics

&

Energy

an international open access journal

TURKISH JOURNAL OF ELECTROMECHANICS AND ENERGY
VOLUME 3 NO 1

Editorial

Special Issue from the ICADET 2017 Conference

June, 2018

It's our pleasure to introduce the third volume of Turkish Journal of Electromechanics & Energy (TJEE). With this volume, we are about to complete third year in raising our child TJEE. This is made possible by our authors, reviewers and editorial board members, and we are grateful for their time, efforts and valuable suggestions.

This special issue of the TJEE (Vol 3. No:1 January-June 2018) consists of five articles selected from the **ICADET-2017 conference** which was held in Bayburt, Turkey during September 21-23, 2017.

First study by **Bolat and Sivrioğlu** investigated active vibration suppression of a flexible blade element using magnetorheological layer patch-electromagnetic actuator. An interaction model of the MR patch electromagnetic actuator was derived and a force characterization was realized, in their work.

Yıldırım and Keleş reported structural properties such as phase relationships, microstructures, and hardness of Co-Cr-Mo biomedical alloys produced by investment casting technique in three different compositions.

Kaya et al. aimed to estimate the amount of power that can be generated using wind turbines in accordance with the wind speed data obtained from Amasra town, using Artificial Neural Networks (ANN) method. The energy generation capacity of Amasra was analyzed for different wind turbines.

A simple method for energy saving in tunnel lighting was studied by **Aksoy**. He examined innovations for illumination and lamp control methods for tunnels, and calculated the amount of energy saving theoretically.

Last study by **Gürdoğan et al.** introduced a multilayered implantable antenna design for medical implant communication system (MICS) band biotelemetry applications. Analysis and design of the antenna was carried out using CST Microwave Studio and the results were validated by means of ANSYS HFSS simulator.

Publishing the special issue was a long and meticulous process. We would like to convey our thanks to Dr. Murat ÇOLAK on behalf of ICADET 2017 Conference Organizers for accepting our invitation to publish a special issue in TJEE. We attended to the conference, and reviewed the presentations that match our journal's aim and scope. We determined 52 presentations among 600+ and invited them to submit their manuscripts for review process in TJEE. 25 manuscripts were evaluated by our reviewers and eventually 9 of those were published in two special issues.

We will continue to our endeavor in archiving and sharing the knowledge with our open-access policy. We acknowledge our publisher's (Science Literature Publishing) support always behind us, and promotion the dissemination of science without barriers. On June 30th , we are deeply saddened by the loss of the distinguished science historian Prof. Fuat Sezgin who devoted his life for archiving the scientific achievements in Islamic world. He passed away at the age of 93, leaving a true legacy behind him.

He started his carrier studying at the Faculty of Letters of Istanbul University, in 1943. He earned his Ph.D on Arabic language and literature from same university in 1950 under the guidance of German Orientalist Hellmut Ritter who helped him to establish his path in science history. He moved to Germany in 1961, and began working as a visiting professor at the University of Frankfurt. He was promoted to professorship in 1965. His efforts in Frankfurt concentrated on Islam's Golden Age of Science. In 1982, Sezgin established the Institute of the History of the Arab Islamic Sciences in Goethe University (Institut für Geschichte der Arabisch-Islamischen Wissenschaften an der Johann Wolfgang Goethe-Universität). that houses the most comprehensive collection of writings on the historical Arabic-Islamic science. In 1983, Sezgin also established a unique museum within the institute, bringing together more than 800 replicas of ancient scientific instruments, tools, and maps, mostly belonging to the Golden Age of Islamic science [1]. He also founded a very similar museum in İstanbul which was inaugurated on 25 May 2008 [2].

Professor Fuat Sezgin

Professor Sezgin next to terrestial globe with world map which seventh Abbasid Caliph al-Mamûn (reigned 813–833 c.e.) commissioned a large group of astronomers and geographers to make. This and many other replicas of medieval age scientific instruments are available at Istanbul Museum of the History of Science and Technology in Islam

Photo credits: Sabah, Turkish Daily Newspaper

*He devoted his life studying and listing scientific contributions made by Muslim scholars throughout history. He prepared 17-volumes "***Geschichte des Arabischen Schrifttums***" (History of Arabic – Islamic Sciences) which is one of the principal sources for the history of science and technology in the Islamic world. As part of his meticulous efforts, he was known to read and understand 27 languages. He was the recipient of several prestigious awards, and member of several academies yet more importantly, he was a great example for young scientists in terms of dedication and curiosity in learning even in his later ages. We plan to commemorate his contributions to the science literature and his legacy.*

References and further reading:

1) https://globintel.com/turkey/fuat-sezgin-bio-biography-age-wife-career-publications-awards-recognition-and-death-1924-2018/

2) https://www.tccb.gov.tr/en/news/542/53656/president-erdogan-receives-prof-fuat-sezgin

3) His biography, http://www.biyografya.com/biyografi/16909

4) The web site of the institute he established "Institut für Geschichte der Arabisch-Islamischen Wissenschaften in Goethe University at Frankfurt" (mainly in German) http://www.uni-frankfurt.de/58601604 , and the museum within it https://www.uni-frankfurt.de/59012099/Museum

5) The web site of Istanbul Museum of the History of Science and Technology in Islam which was dedicated to his work, http://www.ibttm.org/ENG/

6) His publications: https://www.uni-frankfurt.de/58972511/Andere_Themen#Katalog (in English,and German)

http://www.islamtarihikaynaklari.com/index.php/haber-ve-duyuru/378-arap-islam-bilimleri-tarihi-geschichte-des-arabischen-schrifttums-cevriliyor

(in Turkish), Last acces date: 04/07/2018

Editors-in-Chief

Ömer Necati CORA, Ph.D & Mustafa Ergin ŞAHİN, Ph.D

Active Vibration Suppression of a Flexible Blade Element Using Magnetorheological Layer Patch-Electromagnetic Actuator

Fevzi Çakmak Bolat[1*] and Selim Sivrioğlu [2]

[1] Department of Mechanical Engineering, Bayburt University, 69000, Bayburt, Turkey
[2] Department of Mechanical Engineering, Gebze Technical University, 41400, Gebze, Turkey

ABSTRACT   This study proposes a new active control structure to suppress vibrations of a small-scale wind turbine blade with magnetorheological fluid (MR) patch actuated by an electromagnet. An interaction model of the MR patch electromagnetic actuator was derived and a force characterization was realized. A linear quadratic gaussian (LQG) controller was designed using the state space model of the flexible blade element. The LQG controller was experimentally realized by means of the blade structure under the impact load and steady state aerodynamic load conditions. The results of experiments showed that the MR patch is effective for suppressing vibrations of the blade structure.

Keywords: Active Vibration Control, MR Patch Actuator, LQG Control, Flexible Blade

1. INTRODUCTION

Active vibration control system improves the performance of the structures in terms of reduction in vibration amplitude compared to passive systems. Actively controlled flexible structures with embedded piezoelectric (PZT) layers have been studied by many researchers to create smart or adaptive structures for responding on changing external conditions. Although PZT layer has great potentials especially for aerospace applications, there are some difficulties in its realization for large engineering systems.

The magnetorheological fluids are non-Newtonian fluids consisting of ferromagnetic particles that can change its rheological properties under application of an external magnetic field. The MR fluid has distinct properties for engineering applications and can be used in vibration control studies [1-4]. One of the most known engineering applications of the MR fluid is the MR damper used in vehicle suspensions with   semi-active control. In these dampers, the damping force is controlled by changing the viscosity of the MR fluid with applied electric current of a coil inside the damper. The MR fluid was also used in the active vibration control of structural systems [5-6]. Many researchers

examined the behavior of sandwich structures containing MR fluid under a magnetic field and active vibration control [7-9]. Valevate studied the analytical modeling and the potential use of MR fluids for performing semi-active vibration control [10]. Rajamohan et all proposed a semi-active control synthesis which was presented to control the dynamic characteristics of fully and partially treated MR sandwich beams [11]. The governing equations for the motion of a three-layer MR sandwich beam were expressed in the state variable form, and an observer-based linear quadratic regulator (LQR) optimal control strategy was developed. Hirunyapruk performed an adaptive tuned vibration absorber (ATVA) exploiting the changeable properties of MR fluids in the pre-yield state [12]. This ATVA has been experimentally worked with PID control.

In this study, the ferromagnetic feature of the MR fluid is employed for an electromagnet actuator. The MR layer patch is attached on a flexible blade element and attracted by the electromagnet to suppress the vibration of the flexible structure. In this case, the force is generated by the magnetic field of the electromagnet and there is no contact during operation. It is also

possible to use an iron plate as an attracting element for the electromagnet instead of using MR layer patch. Nevertheless, the iron plate in the same volume of the patch is 2.5 times heavier than the MR patch and this may change the natural frequencies of the attached structure. In addition, homogeneity and rigidity of the structure may be deteriorated if a ferromagnetic metal fixed on the flexible structure. Moreover, the MR layer patch is easily formed and may take the shape of the structure when it is attached.

Active vibration control of wind turbine wings is an important research topic and was studied in reference [13]. To implement the proposed MR patch electromagnetic actuator, a small-scale wind turbine blade is selected to suppress modes of vibration. In a wind turbine, when the air flows over the turbine blades with a certain angle of attack, lift and drag forces occur and drag forces cause vibrations on the blade. To reflect the real system disturbances in the experimental system of this study, an aerodynamic load was generated, and the designed controller was tested under such effects.

2. MODELING OF THE BLADE STRUCTURE

The blade structure is produced based on the airfoil with code number SH3055 and characteristics and wind tunnel aerodynamic tests for this airfoil are reported in reference [14]. The airfoil is designed for use on small wind turbines. The blade structure is manufactured by a small wind turbine manufacturer [BRZ Enerji, Istanbul, TR] with an aluminum extrusion machine. The airfoil is made hollow to reduce the weight of the blade as shown in Figure 1(b).

2.1 State-Space Model

The layout of the cantilever blade structure with MR patch layer for control design study is shown in Figure 1(a). Here, x coordinate is related with the longitudinal dynamics and w coordinate shows the direction of vibration of the blade. The force that MR patch generated is shown by f and applied to the beam at the distance x_a. Also, f_d shows the disturbance force applied at the distance x_d. The distance x_s denotes the sensor location. The airfoil of the blade is shown in Figure 1(b). An inertia equivalent rectangular shape is calculated for modeling purposes.

For each vibration mode of the cantilever blade structure, the separated equation of motion is given in Eq.1 [16].

$$\ddot{x}_n(t) + 2\varsigma\omega_n\dot{x}_n(t) + \omega_n^2 x_n(t) = f(t)\psi_n(x_a) + f_d(t)\psi_n(x_d) \quad (1)$$

Where ω_n is the mode natural frequency, ς is the damping coefficient and $\psi_n(\cdot)$ is the mode shape function. The state space equation for each modal behavior is obtained using Equation (1) as follows;

$$\dot{\bar{x}}_n(t) = A_n\bar{x}_n(t) + B_n u(t) + D_{wn} d(t) \quad (2)$$

where $\bar{x}_n(t)$ is the state vector, A_n is the system matrix, B_n is the control input matrix, and $u(t)$ is the control input. The structure of the state vector and matrices are as follows;

$$\bar{x}_n = \begin{bmatrix} x_n(t) \\ \dot{x}_n(t) \end{bmatrix}, A_n = \begin{bmatrix} 0 & 1 \\ -\omega_n^2 & -2\varsigma\omega_n \end{bmatrix},$$
$$B_n = \begin{bmatrix} 0 \\ \psi_n(x_a) \end{bmatrix}, D_{wn} = \begin{bmatrix} 0 \\ \psi_n(x_d) \end{bmatrix} \quad (3)$$
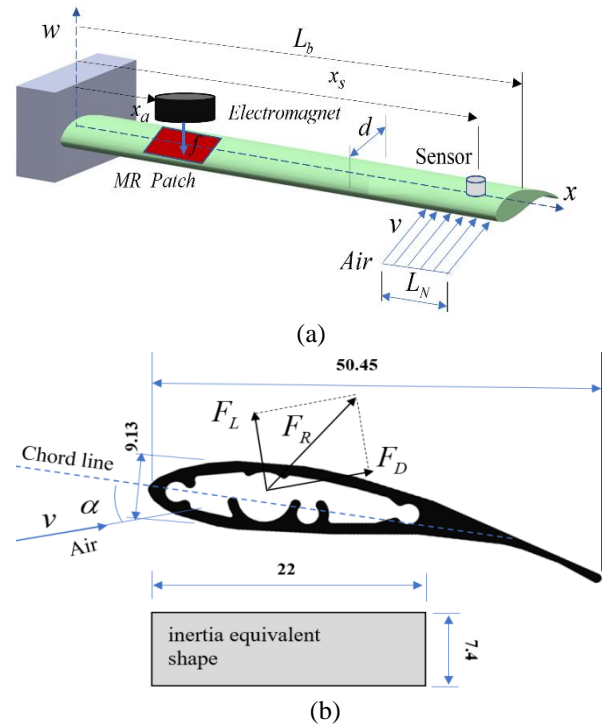

(a)

(b)

Fig. 1. Control system structure; (a) layout of the cantilever blade, (b) airfoil and its inertia equivalent rectangular shape

In distributed parameter systems, the displacement measured by the sensor is modeled as the multiplication of the modal displacement with the mode shape function at the considered point. For the sensor location, the modal output is written as;

$$w(x,t) = \sum_{i=n}^{\infty} x_n(t)\psi_n(x_s) \quad (4)$$

Using Equation (4) the output of the state space equation is obtained for each vibration mode as;

$$y_n = C\,\bar{x}_n(t) = \begin{bmatrix} C_n & 0 \end{bmatrix}\bar{x}_n(t) \quad (5)$$

where the matrix C_n is computed using the following mode shape function.

$$C_n = \psi_n(x_s) = \sinh\beta_n x_s - \sin\beta_n x_s$$
$$- \left[\frac{\sinh\beta_n L_b + \sin\beta_n L_b}{\cosh\beta_n L_b + \cos\beta_n L_b}\right](\cosh\beta_n x_s - \cos\beta_n x_s) \quad (6)$$

Where;

$$\beta_n = \left(\omega_n \sqrt{\frac{\rho A}{EI}} \right)^{1/2} = \left(\frac{2n-1}{2} \pi + e_n \right) \frac{1}{L} \tag{7}$$

If the modeling is extended for N modes ($n = 1, \ldots, N$), the state space structure is obtained as follows;

$$\dot{x}_f = \begin{bmatrix} \dot{\bar{x}}_1 \\ \dot{\bar{x}}_2 \\ \vdots \\ \dot{\bar{x}}_N \end{bmatrix} = \begin{bmatrix} A_1 & & & 0 \\ & A_2 & & \\ & & \ddots & \\ 0 & & & A_N \end{bmatrix} \begin{bmatrix} \bar{x}_1 \\ \bar{x}_2 \\ \vdots \\ \bar{x}_N \end{bmatrix} + \begin{bmatrix} B_1 \\ B_2 \\ \vdots \\ B_N \end{bmatrix} u + \begin{bmatrix} D_{w1} \\ D_{w2} \\ \vdots \\ D_{wN} \end{bmatrix} d$$

$$y_f = \begin{bmatrix} C_1 & C_2 & \cdots & C_N \end{bmatrix} \begin{bmatrix} \bar{x}_1 \\ \bar{x}_2 \\ \vdots \\ \bar{x}_N \end{bmatrix} \tag{8}$$

A reduced order state space model for the control design study can be obtained by considering the first two modes of Equation (8). The reduced order state space equation is written as;

$$\dot{x}_r(t) = A_r x_r(t) + B_r u(t) + D_{wr} d(t)$$
$$y_r(t) = C_r x_r(t) \tag{9}$$

Distributed parameter systems have theoretically infinite number of vibration modes. The state space model obtained as a full model in equation (8) considers certain number of modes. In this study, the full order model of the cantilever blade is built by considering the vibration modes up to 1.25 kHz. In practice, the modal contributions of the higher order modes are inconsiderable due to small modal amplitudes. Also, the reduced order model which contains the first two modes up to 60 Hz is used for controller designs. The frequency responses of the full and reduced order models are shown in Figure 2.
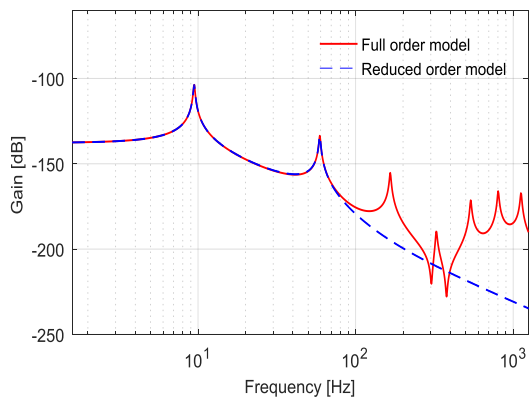

Fig. 2. Frequency response of the blade model

2.2 MR Patch and Actuator System

The MR fluid is filled into the locked plastic bag and glued to ensure that leak-proof as shown in Figure 3. The MR patch stick on the blade with a tape was used to prevent bag flexibility under magnetic field.

The thin plastic bag filled with MR fluid is fixed on the blade element as shown in Figure 4(a). The electromagnet is positioned opposing the MR patch with an air gap over the blade element to apply magnetic field to the MR patch as illustrated in Figure 4(b). When the current is applied to the electromagnet, a magnetic field is created, the iron particles in the MR patch become ordered and an attractive force on the blade is generated so that the vibrations are suppressed. The magnitude of the force depends on the magnetic flux given by the controller based on the displacement information of the blade obtained using an optical sensor in a feedback control structure.
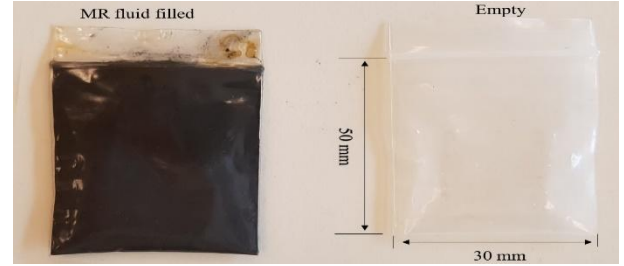

Fig. 3. Structure of the MR fluid patch
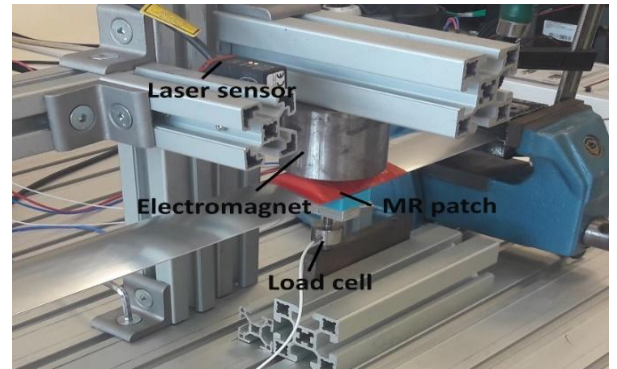
(a)
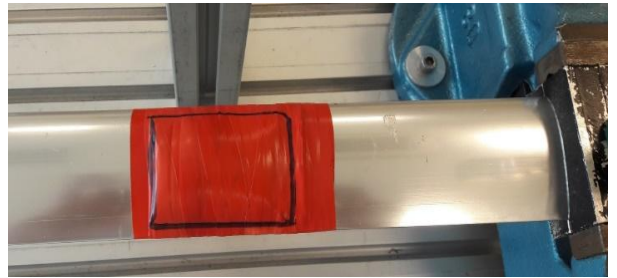
(b)

Fig. 4. (a) Electromagnet and MR patch in the experimental setup, (b) MR patch attached on the blade

2.3 Force Characterization

The interaction between the electromagnet and the MR patch is illustrated as a cross-sectional view in Figure 5. At the initial state as shown in Figure 5(a), the electromagnet is positioned over the blade with an air gap of w_0. When the current is applied to the electromagnet in Figure 5(b), the MR patch is attracted by the electromagnet and an extension of ε is occurred due to flexibility of the plastic bag. At this stage, the blade does not move and the magnetic force and current that extend the MR patch are f_0 and i_0, respectively.

After the extension of the patch is over the MR patch with the blade move toward the electromagnet. The electromagnetic force is defined as;

$$f(t) = k \frac{(i_0 + i_c(t))^2}{\left[w_0 - (\varepsilon + w(t)) \right]^2} \qquad (10)$$

where $k = 1/4\mu_0 N^2 A$. Here, A is the area of the electromagnet, N is the number of the coil turn and μ_0 is the vacuum permeability. Also, i_c is the control current. The electromagnetic force is linearized around (i_0, w_0) values as follows. The system parameters are given in Table 1.

$$f(t) = K_w w + K_i i_c$$
$$K_w = 2k \frac{i_0^2}{w_0^3}, \qquad K_i = 2k \frac{i_0}{w_0^2} \qquad (11)$$
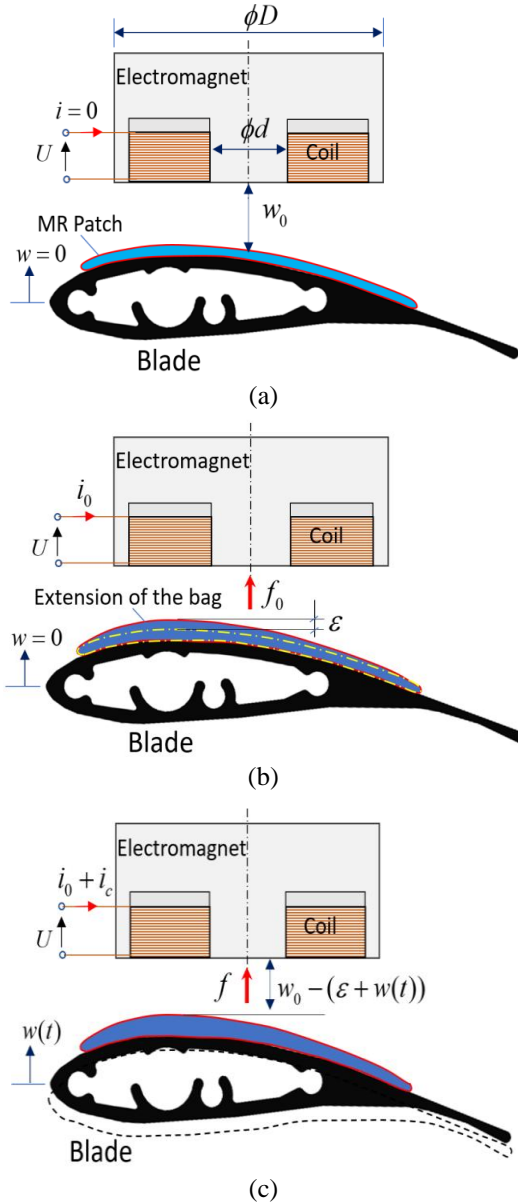

(a)

(b)

(c)

Fig. 5. Interaction model between the electromagnet and the MR patch; (a) initial state (b), extension of MR patch, (c) control of the blade

Table. 1 Values of the blade system parameters

Symbol	Meaning	Value	Unit
L_b	Length of the blade	800	mm
x_a	Distance of the actuator	150	mm
x_s	Distance of the sensor	700	mm
N	Number of the coil turn	221	-
A	Area of the electromagnet	2e-4	mm^2
μ_0	Vacuum permeability	12.5e-6	-
d	Width of the blade	50	mm

Since the MR patch has elasticity at certain extent, the response force of the MR patch layer to the electromagnet force input should be investigated. It is important to show how much electromagnetic force is transmitted to the MR patch. To understand the force variation at the MR patch side a load cell is installed under the blade as shown in Figure 4(a). It is not possible to measure electromagnetic force directly, but the magnetic field can be measured by a gauss meter. The experimental force f_e exerted by the electromagnet obtained using the experimental data with the following equation;

$$f_e = \frac{A}{\mu_0} B^2 \qquad (12)$$

where B is magnetic field measured by using a Gaussmeter. The variations of the experimental forces are shown in Figure 6. In these experiments, the air gap between the electromagnet and MR patch is set to 1 mm. Table 2 also shows the data of the measured experimental forces in different currents. At large coil currents, the loss is increasing as seen in Table 2 and Figure 6.

Table 2. The measured forces in different current

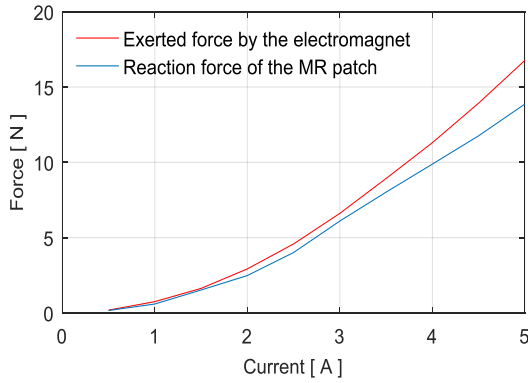| Applied Current (A)	Force at MR Patch side (N) (Measured with load cell)	Electromagnet Force (N) (Measured with Gaussmeter)	Loss %
5	13.87	16.77	17.29
4.5	11.76	13.93	15.57
4	9.88	11.30	12.56
3.5	8.02	8.92	10.08
3	6.10	6.61	7.71
2.5	4.21	4.58	8.07
2	2.56	2.92	12.32
1.5	1.51	1.62	6.79
1	0.63	0.74	14.86
0.5	0.16	0.18	11.11

Fig. 6. Variation of the experimental electromagnetic force and response force exerted by MR patch

2.4 Aerodynamic Load

To test the designed LQG controller under a steady state disturbance, an aerodynamic load effecting on the blade structure is created using an air nozzle. In the case of wind turbines, the air current flows over the wings with a certain angle of attack. Lift and drag forces occur as the air passes over the blades and drag force causes vibrations on the blade. The forces are defined as;

$$F_L = \frac{1}{2} C_L \rho L_N d_b v^2 \quad , \quad F_D = \frac{1}{2} C_D \rho L_N d_b v^2 \qquad (13)$$

where C_L and C_D are lift and drag coefficients. Also, L_N is the air load length, d_b is the width of the blade and v is the relative wind speed. The wing is forced to bend the blade by the effect of aerodynamic drag force F_D. The lift and drag coefficient data of the SH3055 airfoil used in the blade element of this study is given in reference [15]. Using these data, the variation of C_L and C_D with angle of attack is shown in Figure 7.
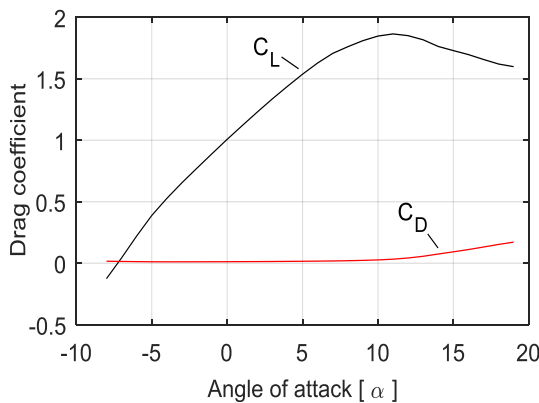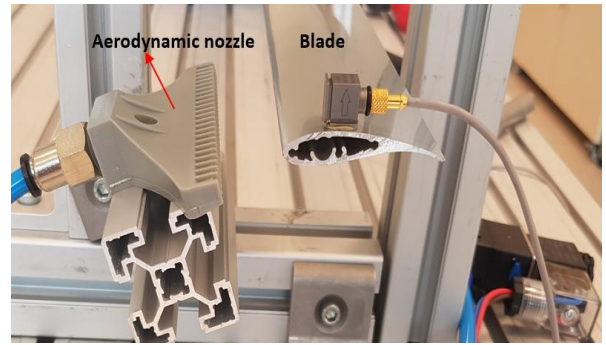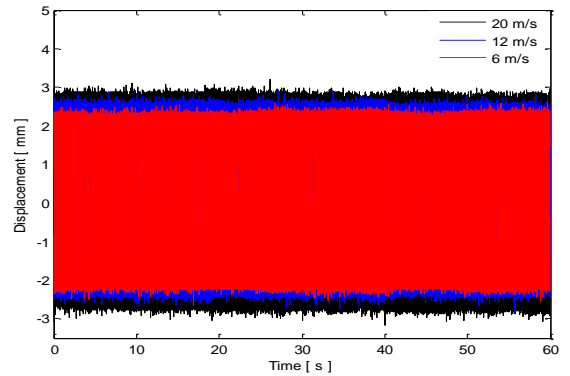

Fig. 7. Aerodynamic load characteristics lift and drag coefficients

(a)

(b)

Fig. 8. (a) Air nozzle effecting aerodynamic load on the blade element, (b) Steady state vibration of the blade element at different wind speeds

An air nozzle is used to create the aerodynamic load in the experimental setup of the blade structure as illustrated in Figure 8(a). Air nozzle blows air to the end of the blade element in adjusted air speeds. In the experimental system, it is observed that the blade starts to vibrate at the angle attack of 14° of the nozzle due to increasing of the drag force on the blade. In this study, the angle of attack of the air nozzle is set to 17.2°. The steady state vibration of the blade element at different wind speeds is illustrated in Figure 8(b).

3. LQG CONTROL DESIGN

LQG control is a modern control design method and it is a combination of the optimal control (LQR) with the optimal state estimation (Kalman filter). The active vibration control system in a feedback structure is shown in Figure 9.
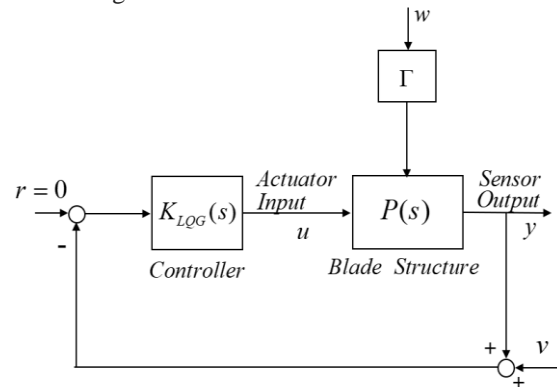

Fig. 9. Feedback control system structure

In general, LQG control improves the time domain responses of the structural vibration systems. The state space model obtained in Equation 11 for the blade element is considered as LQG control design model as follows;

$$\dot{x}_r(t) = A_r x_r(t) + B_r u(t) + D_{wr} d(t) + \Gamma w(t)$$
$$y_r(t) = C_r x_r(t) + v(t)$$
(14)

where $w(t)$ is the system noise and $v(t)$ is the observation noise. These are zero mean, white, uncorrelated Gaussian random signals. The LQG control problem aims to minimize the cost function.

$$J = \lim_{t_f \to \infty} \frac{1}{t_f} E \left[\int_0^{t_f} \left[x^T(t) Q x(t) + u^T(t) R u(t) \right] dt \right]$$
(15)

Where $E\{.\}$ is the statistical expectation operator. Also, Q and R are the weighting matrices applied to the states and control inputs, respectively. The state estimate $\hat{x}_r$ is formed using the Kalman filter state estimator as follows;

$$\dot{\hat{x}}_r(t) = A_r \hat{x}_r(t) + B_r u(t) + K_f (y_r(t) - C_r \hat{x}_r(t))$$
(16)

where K_f is the Kalman filter gain and computed as;

$$K_f = S C_r^T V^{-1}$$
(17)

Here S is the solution of the Algebraic Riccati Equation.

$$A_r S + S A_r^T - S C_r^T V^{-1} C_r S + \Gamma W \Gamma^T = 0$$
(18)

Where V and W are the spectrum of the system and observation noises. The optimal control is formed using the LQR state feedback gain matrix F and the estimated state $\hat{x}_r$.

$$u(t) = -F \hat{x}_r$$
(19)

It is possible to combine the optimal control and Kalman filter by substituting Equation (19) into (16) and arranging in the state space form.

$$\begin{bmatrix} \dot{\hat{x}}_r \\ u \end{bmatrix} = \begin{bmatrix} A_r - B_r F - K_f C_r & K_f \\ -F & 0 \end{bmatrix} \begin{bmatrix} \hat{x}_r \\ y_r \end{bmatrix}$$
(20)

The LQG controller is in the state space form with the following controller matrices.

$$K_{LQG} = \begin{bmatrix} A_r - B_r F - K_f C_r & K_f \\ -F & 0 \end{bmatrix} = \begin{bmatrix} A_k & B_k \\ C_k & D_k \end{bmatrix}$$
(21)

The LQG control block structure is shown in Figure 10. The frequency response characteristics of the LQG controller is depicted in Figure 11. The closed-loop frequency response of the system is presented in Figure 12. The LQG controller suppressed the targeted vibration modes with significant reduction in magnitudes of the blade system.
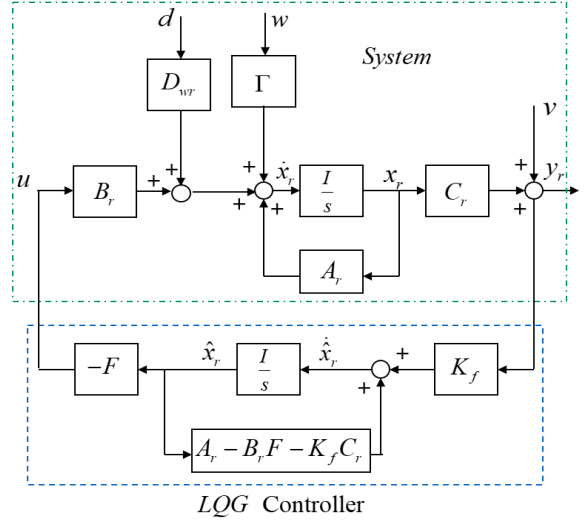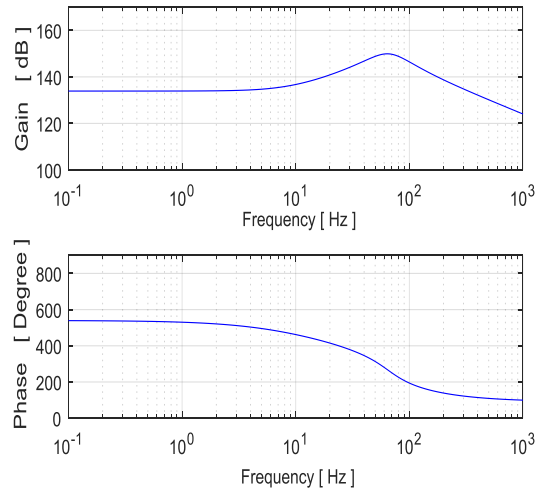

Fig. 10. LQG control structure

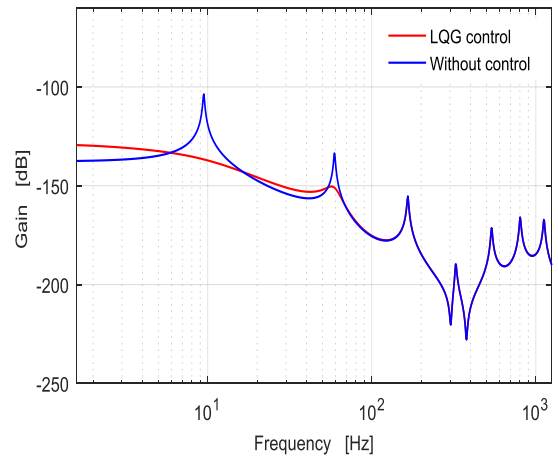Fig. 11. Frequency responses of the LQG controller

Fig. 12. Frequency responses of the closed loop system

4. EXPERIMENTAL SYSTEM

The photo of the experimental system setup is shown in Figure 13. An aluminum alloy 6060 elastic blade which is used in a small-scale wind turbine test system is studied for vibration suppression purposes. A MR patch is attached on the surface of the blade and the blade is fixed at one end using a clamp. In the experimental system, a current drive is used to drive the electromagnet. Vibration analysis of the blade is performed with a Bruel&Kjaer 3053 device. The designed LQG controller is realized using dSpace 1104 control card. The controller is discretized and compiled in the state space form using a Matlab/Simulink file and installed on dSpace control card.
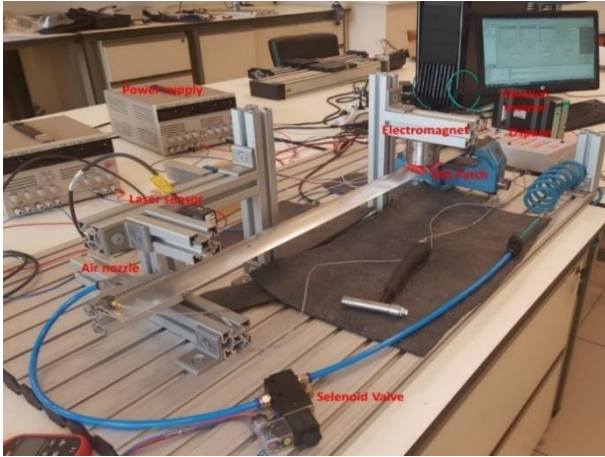
Fig. 13. Experimental system setup

The experimental frequency responses of the closed loop system with the LQG controller is obtained and presented in Figure 14(a). The results of the first two modes for the control design is also shown in Figure 14(b).

(a)

(b)
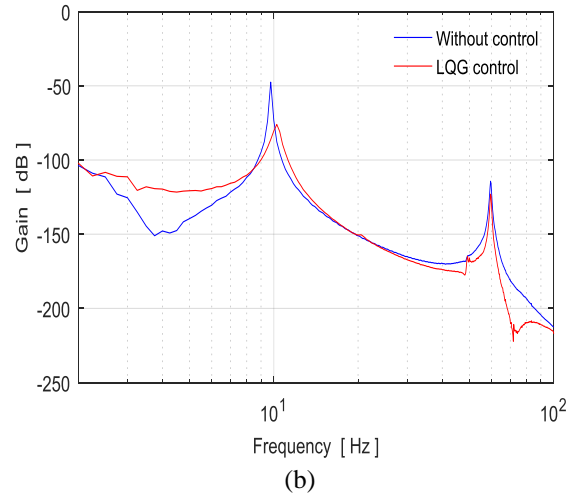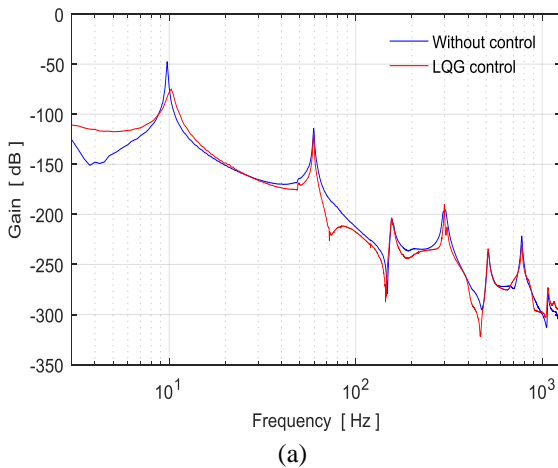
Fig. 14. Experimental frequency responses of the closed loop system; (a) full system, (b) first two modes

Table 3. Amount of reduction in gains with LQG control

Mode Number	Gain reduction [dB]
1st mode	28.55
2nd mode	8.7

The amount of reduction in the closed loop frequency response gain is summarized in Table 3. The LQG controller provided significant gain reduction in the first vibration mode of the blade element. The reduction in the second mode is also at acceptable level. Since an ideal mathematical model is used in the simulation, the frequency response of the closed loop in the simulation shows a smooth significant reduction in gains. In real systems, there are some unmodeled dynamics and the experimental results demonstrate some differences with simulation results. On the other hand, the overall trend in the closed loop frequency responses of the simulation (Figure 12) and experimental (Figure 14) results are in accordance with each other.

(a)

(b)
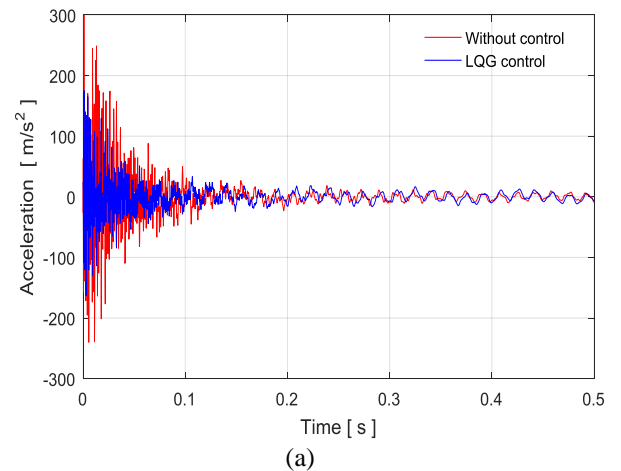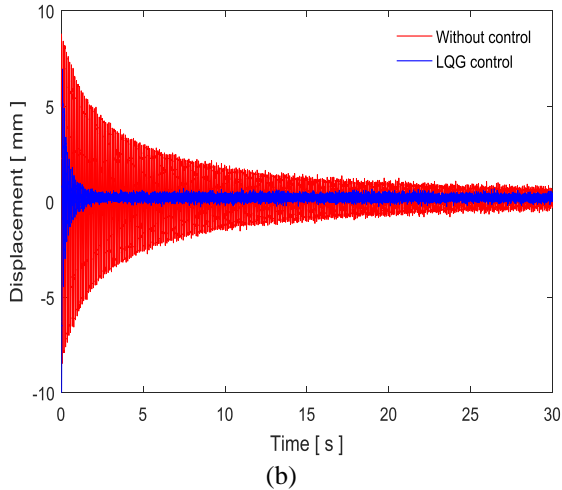
Fig. 15. Experimental time history responses of the closed loop system; (a) acceleration, (b) displacement

At first a transient response analysis is realized with LQG controller. The transient time history responses of the closed loop system with LQG control are shown in Figure 15.

The control effectiveness is good at acceleration and displacement responses. When the air nozzle blows air to the end of the blade element in adjusted air speeds, the blade element starts to vibrate due to drag forces on it. This creates a steady state aerodynamic load on the blade. Note that air speed is taken as 15 m/s in the experiments. The designed LQG controller is tested under the steady state aerodynamic load. Experimental time history responses of the closed loop system for a continuous control case from a starting time are shown in Figure 16. Moreover, the repeated controlled and uncontrolled tests are realized to understand the response characteristics of the controller as given in Figure 17. The controller shows the better control effectiveness to attenuate vibrations of the blade.
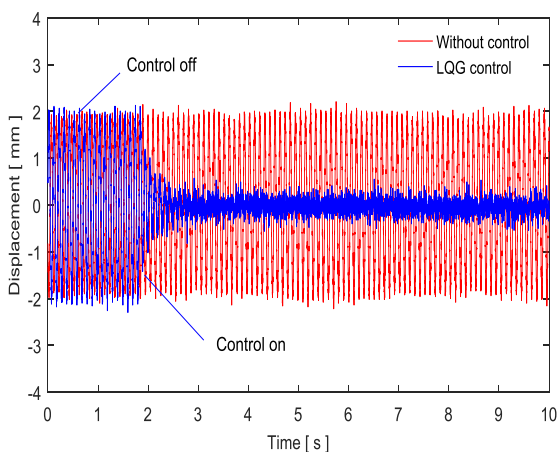

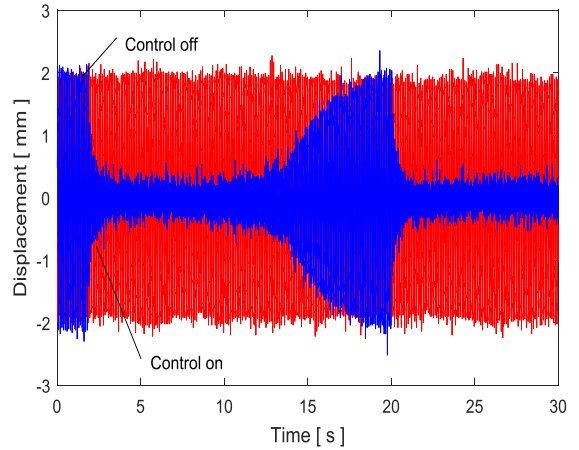Fig. 16. Experimental results of the closed loop system with steady state aerodynamic load

Fig. 17. Experimental results of the repeated controlled and uncontrolled blade vibrations

5. CONCLUSIONS

In this study, vibration of a small-scale wind turbine blade is suppressed using a MR patch layer and electromagnetic actuator under the effect of steady state aerodynamic disturbance. A force based interaction model between MR patch and electromagnet is derived and some characterization works are presented. An LQG controller is designed to attenuate the vibration of the blade structure. Some experiments are realized to show the effectiveness of the proposed MR patch electromagnetic actuator for the transient and steady state aerodynamic loads. The experimental frequency responses and time history responses of the closed loop system demonstrated significant vibration reduction.

References
[1] G. Yang, Large-Scale magnetorheological fluid damper for vibration mitigation: modeling, testing and control, Ph.D. Dissertation, University of Notre Dame, (2001), http://cee.uiuc.edu/sstl/gyang2/ch2.pdf.
[2] B. F. Spencer, S. Nagarajaiah, State of the art of structural control, Journal of Structural Engineering, 129, 845–856, (2003).
[3] Y. L. Xu, W. L. Qu, and J. M. Ko, Seismic response control of frame structures using magnetorheological/electrorheological dampers, Earthquake Engineering and Structural Dynamics, 29, 557-575, (2000).
[4] R. Stanway, J. L. Sproston, A. K. El Wahed, Applications of electrorheological fluids in vibration control: a survey, Smart Materials and Structures, 5, 464-482, (1996).
[5] K. D. Weiss, J. D. Carlson, D. A. Nixon, Viscoelastic properties of magneto-and electro-rheological fluids, Journal of Intelligent Material Systems and Structures 5, 772-775, (1994).
[6] H. Niu, Y. Zhang, X. Zhang, and S. Xie, Active vibration control of plates using electro-magnetic constrained layer damping, International Journal of Applied Electromagnetics and Mechanics, 33(1, 2), 831-837, (2010).
[7] M. Romaszko, Free vibration control of a cantilever MR fluid based sandwich beam. In Carpathian

Control Conference (ICCC), 2013 14th International (pp. 311-314), May, (2013).

[8] B. Hu, D. Wang, P. Xia, & Shi, Investigation on the vibration characteristics of a sandwich beam with smart composites-MRF. World Journal of Modelling and Simulation, 2(3), 201-206, (2006).

[9] L. Chen, & C. H. Hansen, Active vibration control of a magnetorheological sandwich beam, Proc. Acoustics 2005 (Busselton Western Australia), 93-98, (2005).

[10] A. V. Valevate, Semi-active Vibration control of a beam using embedded magneto-rheological fluids, Doctoral Dissertation, Wright State University, (2004).

[11] V. Rajamohan, R. Sedaghati, and S. Rakheja, Optimal vibration control of beams with total and partial MR-fluid treatments, Smart Materials and Structures, 20(11), 115016, (2011).

[12] C. Hirunyapruk, Vibration control using an adaptive tuned magneto-rheological fluid vibration absorber, Doctoral Dissertation, University of Southampton, (2009).

[13] S. A. Fazelzadeh, M. Azadi, and E. Azadi, Suppression of nonlinear aeroelastic vibration of a wing/store under gust effects using an adaptive-robust controller, Journal of Vibration and Control, 23(7), 1206-1217, (2017).

[14] M. S. Selig, and B. D. McGranahan, Wind tunnel aerodynamic tests of six airfoils for use on small wind turbines. Journal of Solar Energy Engineering (Transactions of the ASME), 126(4), 986-1001, (2004).

[15] D. M. Somers, and M. D. Maughmer, Theoretical aerodynamic analyses of six airfoils for use on small wind turbines, National Renewable Energy Laboratory (NREL), (No. NREL/SR-500-33295), (2003).

[16] K. Zhou, and J. C. Doyle, Essentials of robust control upper saddle river, NJ: Prentice Hall, (104), 88-267, (1998).

Biographies

Fevzi Çakmak Bolat received the B.S and M.S. degree in mechanical engineering from the Atatürk University, Erzurum, Turkey, in 2011. He is currently a research assistant and a Ph.D. student at Gebze Technical University Gebze, Turkey. His research interests are modeling and experimental verification of active vibration control, dynamic system modeling and control, semi-active control of smart materials, and robust control applications.

E-mail: fevzibolat@bayburt.edu.tr

Selim Sivrioğlu received the Ph.D. degree from Chiba University, Chiba, Japan, in 1998. He is currently Professor in the Department of Mechanical Engineering, Gebze Technical University, Gebze, Turkey. His current research interests are smart structures, modeling and experimental verification of superconducting magnetic levitation, active control of magnetic bearings, semi-active control of vehicle suspension systems, robust and adaptive control applications.

E-mail: s.selim@gtu.edu.tr

Production of Co-Cr-Mo Biomedical Alloys via Investment Casting Technique

Mehmet Yıldırım[1*], Ali Keleş[1]

[1]Selçuk University, Department of Metallurgical and Materials Engineering, 42075, Selçuklu-Konya, Turkey

ABSTRACT Co-Cr-Mo biomedical alloys with three different compositions were produced by investment casting technique from high purity constituents. The structural properties such as phase relationships, microstructures, and hardness of the alloys were studied. The phase relationships of the samples were investigated using x-ray diffraction and the microstructural characterization were performed using light optical microscopy. It was found that the microstructure of the samples was composed of Co-based dendrites (matrix phase) and carbides (second phase particles) precipitated at grain boundaries and interdendritic regions. These carbides act as strengthening particles in such alloys. Moreover, the mean hardness of these three samples were measured as 24.2, 24.5 and 29.6 HRC. The values were found to be in a good agreement with the optimum hardness value given in the ASTM F75 standards.

Keywords: ASTM F75, Co-Cr-Mo Alloys, Investment Casting Technique,

Cite this article: M. Yıldırım, A. Keleş, Production of Co-Cr-Mo Biomedical Alloys via Investment Casting Technique, Turkish Journal of Electromechanics & Energy 3(1) 12-16 (2018)

1. INTRODUCTION

Co-Cr alloys, which are also known as vitallium steels until the beginning of 1930s, were used as candidates for replacing gold in dentistry. Later, they became one of the three main metallic biomaterials used in orthopedic surgery especially as hip prostheses and internal fixators. Co-Cr based alloys can be classified into two main groups: cast Co-Cr-Mo alloys and hot forged Co-Cr-Ni-Mo alloys. Among these two types of alloys, Co-Cr-Mo alloys have been used for many years in dentistry and recently in artificial joint production. Co-Cr-Mo alloys, also known as ASTM F75, contain 58-69 %Co, 26-30 % Cr, 5-7 % Mo and various elements [1-4]. The high Cr content (25-27 wt %) provide biocompatibility and also contribute to corrosion resistance by forming a protective chromium oxide (Cr_2O_3) layer. Moreover, they also exhibit superior mechanical properties by forming metal carbide precipitates through Mo content (5-7 wt %) [5].

Co-Cr-Mo biomedical alloys can be produced by various manufacturing processes such as powder metallurgy, forging and investment casting technique. Among these methods, investment casting technique is the promising method in the production of implants used in orthopedic surgical operations. The main advantage of investment casting technique compared to other methods is that complex shaped parts at very low cost can be produced with dimensions and tolerances very close to the final dimensions.

Co-Cr-Mo biomedical alloys are extensively used in the production of orthopedic implants due to their attractive strength, hardness, toughness, corrosion and wear resistance [6, 7]. It is well-known that Co-Cr-Mo alloys possess low ductility along with cast defects such as micro porosity, chemical inhomogeneity and large grain size in the as-cast state [8-10]. Their poor ductility could be enhanced with proper heat-treatment and alloying additions [11]. In the literature, the effects of alloying additions have been investigated for Co-Cr-Mo alloys. It was noted that addition of Ni enhances ductility and stabilizes Co matrix phase but it has an important allergy problem for human body on biomedical applications [10, 12, 13]. On the other hand, C addition above a certain limit leads to formation of carbide particles at grain boundaries. These particles can be the source of stress concentration resulting in fracture [10]. Moreover, W addition increases γ-Co (FCC)↔ε-

Co (HCP) allotropic phase transformation temperature and forms W$_3$C which act as strengthening phase [14].

In this study, it was first aimed to produce Co-Cr-Mo biomedical alloys having different Fe contents by investment casting technique and then investigate their structural properties and hardness. In addition, emphasis was placed on the effect of Fe content on phase relationships on microstructures and hardness since commercially pure alloys may contain Fe amount higher than the optimum content according to ASTM F75 standards [2].

2. EXPERIMENTAL

2.1 Production of the Samples

In this study, Co-Cr-Mo alloys with three different compositions were produced by investment casting technique as shown in Figure 1. This technique with ceramic shell method is performed using the following steps; wax modeling, attachment of multiple parts to wax runner, ceramic shell formation by dipping wax parts in a wet ceramic slurry, removal of wax from the mold by autoclave, sintering of the molds, pre-heating prior to casting and casting steps. As the first step, wax models of the parts were created by wax injection machines using industrial green wax. This step is very important because the surface and dimensional characteristics of the waxes dictate the surface and dimensional properties of the products. Multiple wax models were attached to a wax runner. The wax models were positioned at a proper angle for smooth flow of the melt during casting on the wax runner to prevent the formation of turbulence. Then, two different ceramic slurries were prepared for the ceramic shell formation. Then, wax runner was left to dry at atmospheric conditions. After drying, the wax is removed in an autoclave at 175 °C under 7-8 bar water vapor pressure for 15 minutes leaving the ceramic mold as a residue. Since the ceramic molds did not have sufficient thermal and mechanical strength, they were heated only to a temperature around 700 °C. At this temperature, the ceramic molds were fired for 4 hours in order to be sintered and remove the wax residuals.

Then, molten metal was poured into the hot ceramic molds. During this process, Ar gas was blown through the surface of the molten metal to prevent direct exposure of the

melt from air. The casting temperature was set as 1585 °C and casting was performed with an induction furnace having 25 kg capacity. After casting, parts were left cooling under ambient condition. The ceramic molds were then broken by vibration or hammer. Finally, individual parts were cut from the runner.
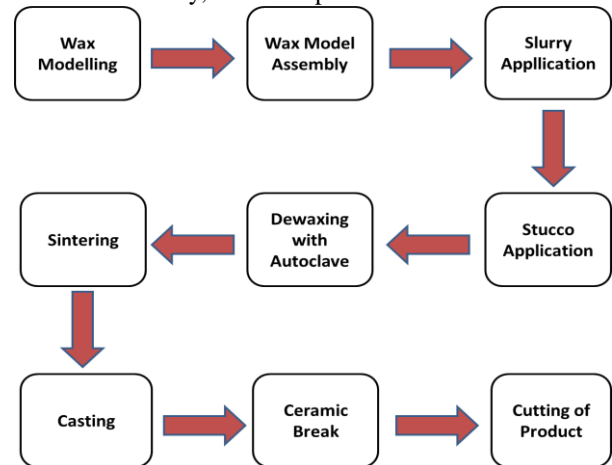

Fig. 1. Schematic pattern of the production of the samples via investment casting technique

2. 2 Characterization

The chemical compositions of the Co-Cr-Mo samples were tested using Oxford Foundry Master Model optical emission spectrometer. The structural characterization, by means of phase analysis and crystal structure, for Co-Cr-Mo alloys produced by the investment casting technique were carried out using X-ray diffraction (XRD) analyses. XRD analyses were conducted using a Bruker D8 Advance model diffractometer with Cu-Kα radiation (λ = 1.54056 Å) and an X-ray source operating voltage of 40 kV. XRD scans were performed in the 2θ range of 25°–100° using a scanning rate of 2°/min. Samples for microstructural examination were mechanically grinded (with 120-1200 grit SiC papers), and then polished with Al$_2$O$_3$ suspension. Then, samples were electrolytically etched with chromic acid solution at a voltage of 4 V for 12 s. Rockwell-C hardness measurements were performed using a Digirock RBOV Hardness tester. The mean hardness values were determined by averaging eight measurements obtained for each sample.

3. RESULTS

Table 1. Chemical composition of investigated Co-Cr-Mo samples from optical emission spectroscopy analysis (wt%) and chemical compositions according to the ASTM F75 and ISO 5832-4 Standards

Sample	Co	Cr	Mo	Fe	Ni	W	Mn	C	Si
Sample 1	64.3	28.0	5.5	0.404	0.0775	0.107	0.457	0.206	0.731
Sample 2	64.9	27.6	5.33	0.728	0.0749	0.0868	0.283	0.206	0.673
Sample 3	64.0	28.6	5.0	1.0	0.0945	0.0635	0.298	0.183	0.656
ASTM F75	balance	27-30	5-7	max. 0.75	max. 0.5	max.0.2	max. 1	max. 0.35	max. 1
ISO 5832-4	balance	26.5-30	4.5-7	max.1	max. 1	max.	max. 1	max. 0.35	max. 1

The chemical compositions of the investigated samples are given in Table 1. The results of the chemical analysis of the alloys indicated that the Fe concentration for the Sample # 1 and 2 were below than maximum Fe concentration of ASTM F75 standards [2], while the Fe concentration of the Sample 3 (1 %) was higher than the maximum allowable value (0.75 %). Nevertheless, Sample 3 shows agreement with the ISO 5832-4:2014 [3] standards.

The concentrations of Co, Cr and Mo, on the other hand, were in the designated range specified by ASTM F75 and ISO 5832-4:2014 standards. Furthermore, the amount of Ni, which is an important parameter in these alloys, is less than 0.1% for all three samples. According to the ASTM F75 Standards maximum Ni concentration should be 0.50 %. Although Co-Cr-Mo alloys with high Ni content are used more frequently in leg and arm joints due to their higher load capacity than

that of lower Ni content, high Ni content may lead allergies and poisoning. In addition, especially magnetic resonance (MR) may cause serious problems due to Ni's magnetic property [15].

The XRD patterns of produced Co-Cr-Mo samples were shown in Figure 2. According to the XRD patterns, all the samples were mainly composed of γ-Co phase with a FCC crystal structure [16]. Besides that, presence of low intensity diffraction line corresponding to the (101) plane of ε-Co phase indicated that all samples contain small amount of ε-Co phase with HCP crystal structure [16, 17]. Neither any additional diffraction line nor any shift of the present γ-Co and ε-Co peaks were observed. Nevertheless, Cr has an extended solid solubility in Co and forms a single phase solid solution even at 37 wt% Cr addition [18]. Thus, any diffraction line corresponding to the Cr or Co-Cr intermetallic compounds were observed in XRD analyses.
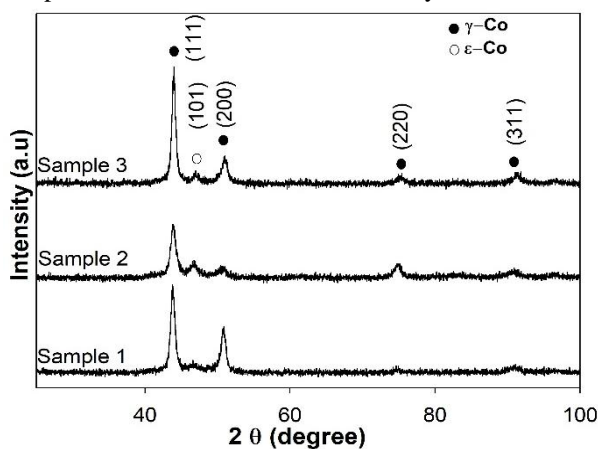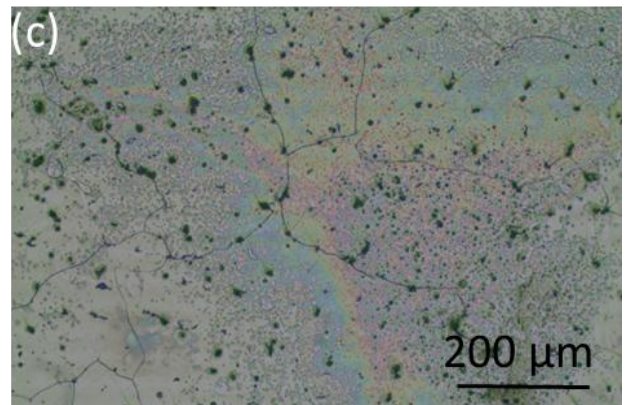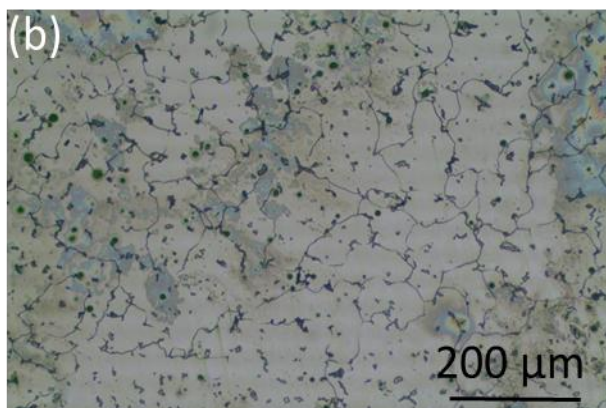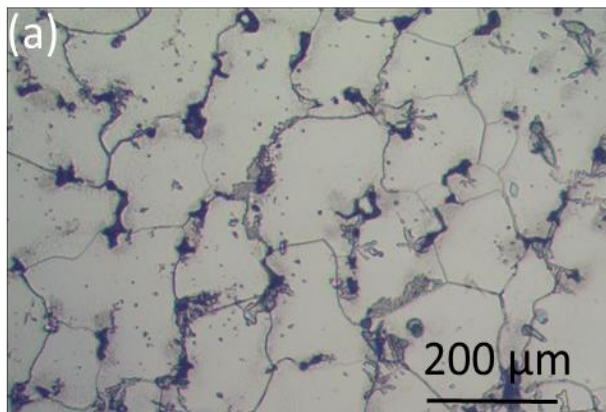

Fig. 2. XRD patterns of Co-Cr-Mo alloys

Fig. 3. Optical micrographs of Co-Cr-Mo alloys, (a) Sample 1, (b) Sample (2), and (c) Sample 3

In addition, lattice parameters of the investigated samples were calculated by applying well-known Bragg's Law and the results were tabulated in Table 2. Pure Co has a lattice parameter of 3.545 Å according to the [16], and the calculated lattice parameters for investigated samples were much higher than that of pure Co. The reason for the higher lattice parameter is the atomic radius differences among constituent elements. Atomic radius of Fe (1.24 Å), Ni (1.25 Å) and Cr (1.25 Å) are very close to that of Co (1.25 Å), while Mo (1.36 Å) and W (1.37 Å) have much higher radius values compared to Co. Normally, the lattice parameter of the FCC γ-Co phase (3.56 Å) in Co-Cr-Mo alloys is very similar to the lattice parameter of pure Co (3.545 Å) [19]. This similarity is due to the almost same atomic radius of Co and Cr. It is well-known that Co is the solvent existing in highest quantity in the alloy (~64%), while Cr is the main solute element (~28%) soluble in Co. Nonetheless, commercially available high purity alloys containing several elements such as Fe, W, Mn, Ni, Si and C were used in this study. Dissolution of these elements increased the lattice parameter of FCC lattice [19]. Nevertheless, when lattice parameters of investigated samples were compared, it was observed that lattice parameter decreased with increasing Fe content. According to the Table 1, amount of Mo and W decreased with increasing Fe content. It is believed that Fe atoms mainly replaced Mo or W atoms in the FCC lattice because Fe, Mo and W all have BCC crystal structure. Moreover, Mo and W have much larger atomic radius compared to Fe and lattice parameter decreased with increasing Fe.

Table 2. Calculated lattice parameters of γ-Co phase in Co-Cr-Mo alloys

Sample	Lattice Parameter (Å)
Sample 1	3.5739
Sample 2	3.5684
Sample 3	3.5600

Figure 3 shows optical micrographs of all produced samples. The microstructures of the investigated samples were consisted of Co dendrites and fine precipitates at grain boundaries and interdendritic zones. All samples showed similar microstructural features with slight differences in size and volume fraction of existing phases. The FCC γ-Co phase is the matrix

phase of the Co-Cr-Mo alloys and the hardness and strength of this alloy are provided by the $M_{23}C_6$ type precipitates. Moreover, some amount of casting defects were also observed for all samples.

The hardness data for all three Co-Cr-Mo alloys are listed in Table 3. The hardness values are increased with Fe content increment in all samples. For Sample 1 and 2, having Fe content of 0.404 and 0.728, respectively, the mean values were close to the lower limit for the required hardness specified in ASTM F75 standard [2]. The lower limit is 25 in HRC where samples 1 and 2 attained hardness values of 24.2 and 24.5 HRC, respectively. Sample 3, on the other hand, suffices the ASTM F75 Standards requirement with 29.6 HRC value [2].

Table 3. Rockwell-C hardness values of Co-Cr-Mo alloys

Sample	HRC
Sample 1	24.2
Sample 2	24.5
Sample 3	29.6

4. CONCLUSION

In this study, biomedical grade Co-Cr-Mo based alloys with chemical compositions per ASTM F75 standard were successfully produced using precision casting technique for orthopedic surgical applications. XRD analyses indicated that all samples had FCC γ-Co single phase. The lattice parameters decreased with increasing Fe content. Finally, the hardness measurements showed that Sample 3 met the ASTM F75 Standards (25 to 35 HRC), whereas Samples 1 and 2 exhibited hardness values very close to the lower limit of the standard.

This study reveals promising properties of the Co-Cr-Mo biomedical alloys. It is predicted that mechanical properties of these alloys at ambient condition can be further enhanced by proper heat-treatment which will control the microstructural features such as Co matrix phase, size, morphology and amount of carbide particles.

References
[1] J. R. Davis, Handbook of materials for medical devices ASM international materials park, (2003).
[2] ASTM F75-12 Standard: Co-28Cr-6Mo Alloy castings and casting alloy for surgical implants, (2012).
[3] ISO 5832-4 Standard: Implants for surgery-metallic materials - Part 4: Cobalt-chromium-molybdenum casting alloy, (2014).
[4] J. A. Disegi, R. L. Kennedy, and R. Pilliar, Cobalt based alloys for biomedical applications ASTM STP 1365 West Conshohocken, PA, (1999).
[5] B. P. John, and K. K. Young, Metallic Biomaterials, Biomedical Eng. Handbook, Unit:37, USA, (2000)

[6] L. Z. Zhuang, and E. W. Wagner, Effects of cooling rate control during the solidification process on the microstructure and mechanical properties of cast Co-Cr-Mo alloy used for surgical implants, J. Mater. Sci., 24(2), 381-388, (1989).
[7] J. F. Bates, and A. G. Knapton, Metals and alloys in dentistry, Inter. Metals Rev., 22(1), 39-60, (1977).
[8] L. Shi, O. D. Northwood, and C. Zhengwang, The properties of a wrought biomedical cobalt-chromium alloy, J. Mater. Sci., 29(5), 1233-38, (1994).
[9] F. B. Pickering, Physical Metallurgy and Design of Steels, Applied Science, Essex, UK, 10-22, (1978).
[10] S. H. Lee, E. Takahashi, N. Nomura, and A. Chiba, Effect of heat treatment on microstructure and mechanical properties of Ni- and C-Free Co-Cr-Mo alloys for medical applications, Mater. Trans., 46(8), 1790-1793, (2005).
[11] J. V. Giacchi, C. N. Morando, O. Fornaro, and H. A. Palacio, Microstructural characterization of as-cast biocompatible Co-Cr-Mo alloys, Material Characterization, 62, 53-61, (2011).
[12] T. Matkovic, P. Matkovic, and J. Malina, Effects of Ni and Mo on the microstructure and some other properties of Co-Cr dental alloys, J. Alloys Compd., 366, 293-297, (2004).
[13] L. Shi, O. D. Northwood, C. Zhengwang, Alloy Design and Microstructure of a Biomedical Co-Cr Alloy, J. Mater. Sci. 28(5), 1312-1316, (1993).
[14] C. D. Orpis, R. Liu, M.x. Mao, and X.J. Wu, Development of stellite alloy composites with sintering/HIPing technique for wear-resistant applications, Materials Design, 28, 581-591, (2007).
[15] J. C. Setcos, A. B. Mahani, L. Di Silvio, I. A. Mjör, and N. H. F. Wilson, The safety of nickel containing dental alloys, Dental Materials, 22(12), 1163-68, (2006).
[16] JCPDS Database, International Center for Diffraction Data, Swarthmore, USA, PDF 15-0806.
[17] JCPDS Database, International Center for Diffraction Data, Swarthmore, USA, PDF 05-0727.
[18] M. Hansen, and K. Anderko, Constitution of binary alloys, McGraw-Hjll, New York, (1958).
[19] K. Yoda, Suyalatu, A. Takaichi, N. Nomura, Y. Tsutsumi, H. Doi, S. Kurosu, A. Chiba, Y. Igarashia, and T. Hanawa, Effects of chromium and nitrogen content on the microstructures and mechanical properties of as-cast Co–Cr–Mo alloys for dental applications, Acta Biomaterialia, 8(7), 2856-62, (2012).

Biographies

Mehmet YILDIRIM was born in Ereğli-Konya, Turkey. He received his BSc. and PhD degrees from Department of Mechanical Engineering, Dokuz Eylul University, İzmir, Turkey in 2004 and from Department of Metallurgical and Materials Engineering, Middle East Technical University, Ankara, Turkey in 2014, respectively. He currently works as an assistant professor at Department of Metallurgical and Materials Engineering, Selcuk University, Konya, Turkey.

E-mail: ymehmet@selcuk.edu.tr

Ali KELEŞ was born in Ilgın-Konya, Turkey. He graduated from Metallurgical and Materials Engineering from Fırat University at Elazığ, Turkey in 2015. He is currently a M.Sc. student at Department of Metallurgical and Materials Engineering, Selçuk University, Konya, Turkey.

E-mail: ali.keles1@outlook.com

A Simple Method for Energy Saving in Tunnel Lighting

Alkan Aksoy

Sürmene Abdullah Kanca Vocational School, Karadeniz Technical University, Trabzon, 61100, Turkey

ABSTRACT Number of highway tunnels continues to increase reducing transport times and costs around the world. As the length of the tunnel increases, the consumed electricity increases also. The biggest chunk of energy is used for tunnel interior luminance. While the tunnels are generally illuminated by sodium vapor lamps, light emitting diodes (LED) based are being increasingly practiced in recently constructed tunnels. In this study, innovations for illumination and lamp control methods for tunnels are examined and the amount of energy savings was theoretically calculated by a simple control method.

Keywords: Illumination, Tunnels, Energy Saving, Lighting Control, Lighting Control Interface

Cite this article: A. Aksoy, A Simple Method for Energy Saving in Tunnel Lighting, Turkish Journal of Electromechanics & Energy 3(1) 17-21 (2018).

1. INTRODUCTION

Electricity consumed for lighting reaches 40% of total electricity consumption in some cities [1]. Electricity consumption in Turkey was reported to be 278.3 TWh approximately in 2016 [2]. Street and tunnel lighting corresponds to 2 to 4.6 % of all electricity consumption in Turkey [3]. High-pressure sodium vapor (HPS) lamps, low pressure sodium vapor lamps (LPS), and light emitting diode (LED) lamps are used for illumination purposes. The use of mercury vapor lamps for lighting has reduced due to their heavy metal content. The use of LED lamps has been increasing around the globe in recent years. The most important reason for this change is the high illumination efficiency of LED lamps. The number of lamps used in the lighting in the tunnels, and the level of the road luminance vary with the lighting level at tunnel exit and the speed of the vehicle. On the other hand, braking distance depends on the speed of the vehicle, the wetness of the road surface, and the highest road slope value of the tunnel [4]. The changes of the brake distance according to the vehicle speeds are shown in Table 1 [5].

The tunnel is divided into zones, and each zone has a different luminance level. These regions are called as the outer (access) zone, the entrance (threshold) zone,

the transition zone, the interior zone, and the exit zone, as shown in Figure 1 [6].

Table 1. Brake distance according to road condition and vehicle speed

Road Condition	Vehicle Speed (km/hour)		
	90	110	130
	Break Distance (meter)		
Wet	90	120	160
Dry	120	160	220
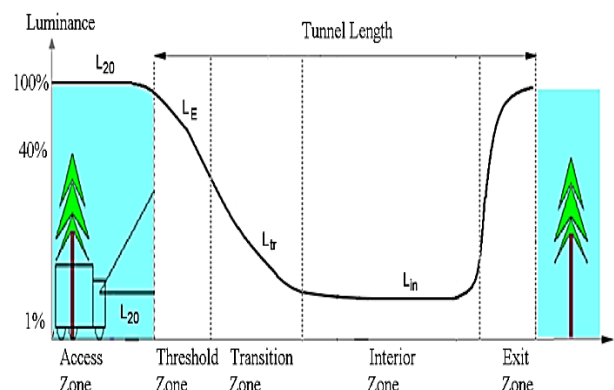
Fig.1. Zones of tunnel based on luminance level

The interior zone of the tunnel has the least luminance compared to the other zone. The luminance in this zone is same and the distance between the lamps is fixed. The average road surface luminance level of the interior zone varies from 1.5 cd/m^2 to 10 cd/m^2 according to the vehicle speed and the number of vehicles as shown in Table 2 [7].

Table 2. Luminance level of interior zone of tunnel

Break Distance	The number of cars (NoC) passing in an hour		
	NoC <100	100< NoC <1000	1000< NoC
160 m	5 cd/m^2	10 cd/m^2	10 cd/m^2
100 m	2 cd/m^2	4 cd/m^2	6 cd/m^2
60 m	1,5 cd/m^2	2 cd/m^2	3 cd/m^2

Adjusting luminance of roads depending on the braking distance saves electricity [8]. Braking distance is highly affected by weather conditions (dry vs. wet road surface). For this reason, the luminance level should be selected carefully in rainy weather conditions.

2. TUNNEL LIGHTING TYPES

Most of the traffic accidents happening in tunnels occur at either entrances or at exits of the tunnels. One of the reasons of the accident is that the human eye cannot quickly adapt to the darkness. This event is called the "*black hole*" effect. The human eyes cannot adapt to light instantaneously when the light level falls below 1/3 of previous level. On the other hand, the human eyes are easy to adapt to bright light. The luminance of the access and exit zone is important for better vision. Luminance of the exit zone should be at least 1/5 of luminance of the outside of tunnel. The luminance level in the tunnels is defined in the CIE (International Commission on Illumination)-88 standard. The selection and installation of the lighting lamps vary based on the length of the tunnel. Common lamp installations are shown in Table 3 [9].

The luminance level of outer zone is measured by photometer. In addition, the number of vehicles is determined by the instant light change obtained data from the photometer. Generally, high-pressure sodium lamps are used in the tunnels. These lamps have ballasts and power setting ranges are not flexible. Contrarily control of LED lamps is very flexible. These two types of lamps compete with each other and the market share of HPS lamps continues to decline. [10]. Besides, induction lamps (IND) which have very little maintenance cost, can be considered as an alternative as these lamps have advantages including light efficiency (LE), long life, simplicity and operating costs. Nevertheless, they contain ballast and mercury in small quantity. The production costs of LED lamps are decreasing and the light efficiency is increasing day by day. High pressure sodium lamps are widely used in rural area lighting because of their low cost. Metal halide lamps are used indoors and outdoors such as sports fields, museum due to the high color rendering index and high light efficiency factor.

Table 3. Advantage and disadvantage of lamp installations

Installation Type & Location	Advantages	Disadvantages
	Best lighting, glare limited	Heavy installation, workmanship
	Low-cost installation, and maintenance	Two ways must be closed in fault
	Easy access, and one way closed in fault	Low use factor, high glare factor
	Low-cost for installation, and maintenance	Blocking of ceiling light by high cars
	Easy installation and maintenance and ways open	Insufficient lighting, temporary

Technical specification of these lamps is shown in Table 4.

Table 4. Technical specification of lamps used in tunnels

Feature	IND Lamps	LED Lamp	Sodium HPS	Metal Halide
Illumination	Sudden	Sudden	5 min	5 min
Lifespan (hr)	100K	50K	24K	10K
Mercury (mg)	5	0	50	1000
LE (lm/W)	80	150	120	110
CRI	80	75	21	64
Consumption	Low	Low	High	High
Oscillation	None	None	Yes	Yes
Maintenance	Low	Low	High	High
Light Level Control	%50	%100	%50	%75

3. LIGHTING CONTROL INTERFACE

The tunnels are usually controlled by supervisory control and data acquisition (SCADA) software. Lamps, ventilation and values of luminance of access zone are controlled and detected by this system. Luminance of all regions except the interior zone of tunnel is different at daylight and night time. The luminance level of the access, transition and exit zones are adjusted from control center based on the information obtained from the photometer [11]. The efficiency factor of the light sources and the saving potential in tunnel are shown in Figure 2 and 3 [12, 13].
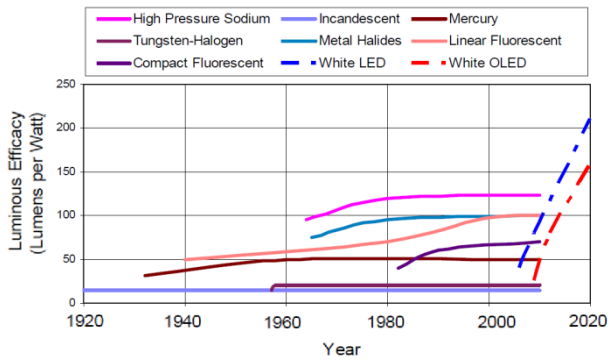
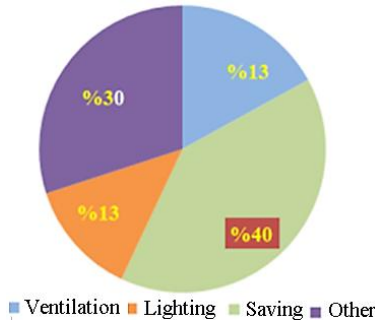Fig. 2. Efficiency factor of the light sources by years

Fig. 3. Tunnel electricity consumption components and saving potential

Besides, data communication for lamp controlling is carried out via cable or wireless communication. Advantages and disadvantages of control interfaces are discussed below and compared in Table 5.

Table 5. The control interfaces of tunnel lamps

Feature	DSI	DALI	Wi-Fi
Setup difficulty	Low	Medium	High
Change difficulty	High	High	Low
Control distance	≤300	≤100	≤90
Number of controlled device	1	≤64	≤255
Independent control	None	Yes	Yes
Transmission media	Cable	Cable	Air

Digital Serial Interface (DSI): It was developed in 1992. Control information is transmitted by cable. The controller uses an 8-bit "*Manchester*" code for communication. The DSI units control the lamps with a DC supply of between 1 and 10V. For example; 1V means 10% of maximum light. Maximum length of control cable is average 100 meters and communication is single way. One DSI unit can control all the lamps of the interior zone [14].

Digital Addressable Lighting Interface (DALI): It is an advanced form of DSI. The difference from DSI is that many different companies' light sources can be controlled together from a single control system. 64 lamps can be controlled separately with the DALI interface. Maximum length of control cable is 300 meters (average). Other units, such as, ventilator, auxiliary lighting, air conditioning (HVAC), alarm signal etc. are controlled by adding other modules (KNX, LON) to DALI control system [15].

Control with Wireless Network: Wireless communication technologies, such as Wi-Fi, are also used in lighting applications [16]. A sample schematic of the LED lamps that can be controlled with Wi-Fi is given in Figure 4.
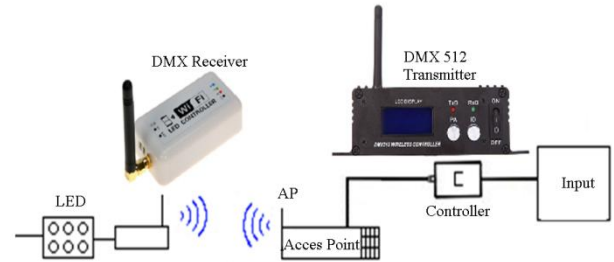

Fig. 4. Wi-Fi control equipment for lamps

4. PROPOSED METHOD FOR LIGHTING SAVING

The number of vehicles that pass through tunnels at night is usually less than the daytime. But lamps in interior zone are on all the times. This situation is not sustainable for energy saving. It is possible to save energy by pulling luminance to lowest level of CIE-88 standard when the vehicles are not in the tunnel zones at nights. The proposed control flow diagram for saving is shown in Figure 5. This method also helps to lower the joint temperature of the LED lamps. As a result, lifetime of LED lamps will increase.
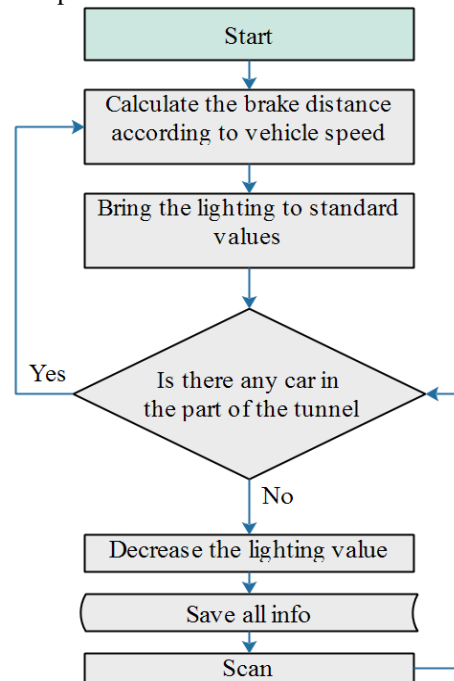
Fig. 5. Suggested flowchart for power saving

As a case study, Araklı Tunnel in Trabzon, Turkey was studied. The speed limit of the Araklı tunnel which is shown in Figure 6 is 80 km/h, and the total length is 1900 meters. The length of the interior zone which is shown Figure 7 is about 1600 meters, 160 lamps are positioned symmetrically totally. There are two 150 watt E-40 lamps in single armature. The luminance value of interior zone of the tunnel is 4.84 cd/m^2. This luminance level is kept throughout the tunnel. The amount of electricity consumed is 100 kW per hour and 825 MW per year. Total electricity consumption in 2015 is 289.960 TL (≈ 100.000 $) as shown in Figure 8 [17].

Fig. 6. Access zone of tunnel

Fig. 7. Interior zone of tunnel

Fig. 8. Electricity consumption by tunnel lighting by years

The number of vehicles passing through the tunnel on years is shown in Figure 9. Number of vehicles passing through the tunnel between 4:00 a.m. and 5:00 a.m. is about 30, and shown in Figure 10 graphically in order to two different days in March 2016.

Braking distance of the vehicles is chosen 160 meter in current study. Interior zone of the tunnel is divided into 10 groups. The representation of these lighting groups is shown in Figure 11.
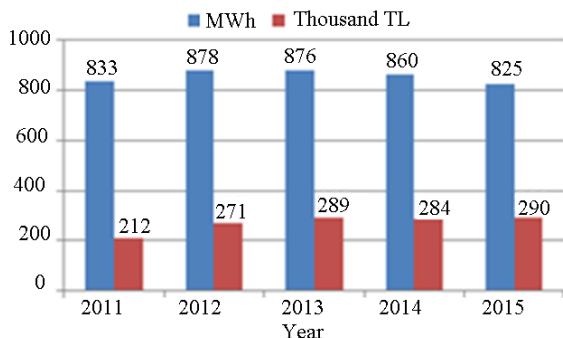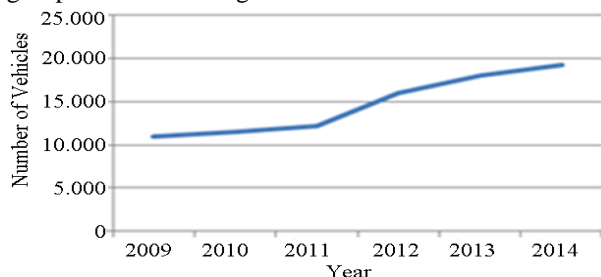

Fig. 9. Total number of vehicles pass through the Araklı tunnel by years
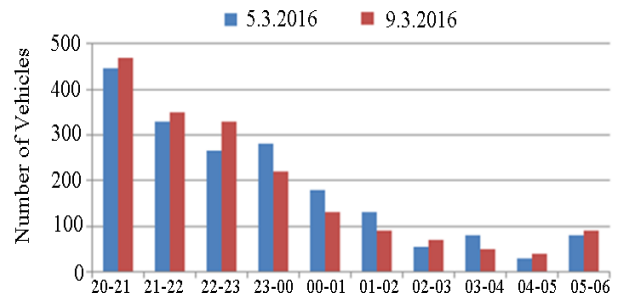
Fig. 10. Number of vehicles passes through tunnel during night time at two different dates
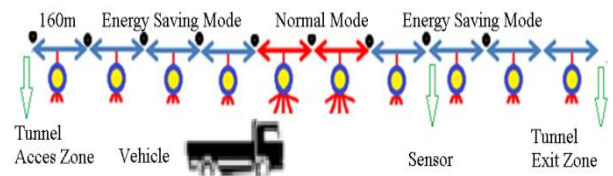
Fig 11. Representation of ten groups of the inner part of the tunnel

It was assumed that the car speed is 82 km/h and has passed all 10 lighting groups in 70 seconds. The lamps are controlled by sensors at the beginning of groups. The luminance of the two groups in front of the car is increased when the car enters into the next lighting group zone. The normal illuminated road length varies between 160 and 320 meters. A 75 Watt LED lamp was used instead of a 150 watt HPS lamp for efficiency. The use of LEDs allows the use of low power and cheaper in selecting power supply and generator.

A car can only affect two groups of lights while in tunnel-saving mode. Therefore, the other interior lamps of the tunnel are in saving mode. The control scheme of luminance of interior zone is shown in Figure 12.
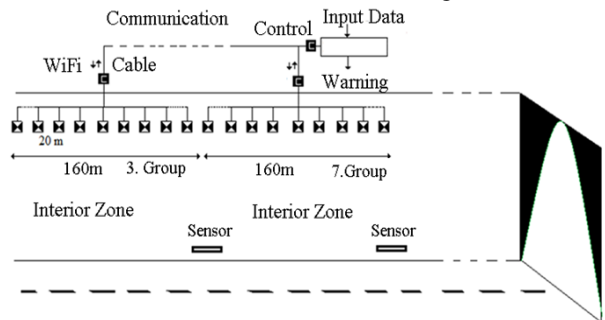
Fig. 12. The lamp control scheme of interior zone of tunnel

Saving rates and electricity consumption of interior zone are shown in Table 6. As it can be seen, the saving can be as high as 70 % when LEDs are used with half and full control.

Table 6. Savings rate between 4:00 am and 5:00 am

Operation Mode	Without Control (Full Power)		With Control (Full and Half)
Lamp type	Sodium	LED	LED
Energy (kWh)	24	12	7,2
Working time	70 sec	70 sec	14 or 56 sec
Saving rate	None	%50	%70

In addition, there are different ways to increase energy savings in long tunnels [18]. For example, lamps can be controlled individually with different control algorithms [19]. In addition, the road brightness value of the interior zone can be adjusted according to the vehicle speed of the road [20]. On the other hand, the problem that may arise in the detectors will adversely affect the luminance. When a problem is encountered, the level of luminance should remain constant at nominal level.

5. RESULTS

In this study, a simple control method is proposed to reduce energy consumption in tunnel illumination. The amount of annual savings is calculated theoretically for a number of vehicles that pass through Araklı Tunnel between 4-5 A.M. hours. Saving rate can further be increased by other control methods. The use of different types of lamps together for efficiency and economy is another solution that can be implemented. On the other hand, high power LED lamps are still expensive nowadays and their efficiencies are still under development. In addition, maintenance costs of tunnels other important factor. Also security should never be compromised while energy saving is achieved in consumption especially at speeds over 80 km/h of cars. Therefore, road lighting on accidents that may occur in tunnels should not be an element that creates an accident.

References

[1] Smart Cities Council, Smart Street Lighting 101: How advanced street lighting systems can transform cities in remarkable ways, (2015).

[2] Information Center, Republic of Turkey Ministry of Energy and Natural Resources, http://www.enerji.gov.tr/tr-TR/Sayfalar/Elektrik, (Last access date: 02/05/2018).

[3] S. Kılavuz, LED road lighting and energy efficiency, 9th National Lighting Congress in Izmir, Turkey, (2013).

[4] K. İzbek, Brake Distance in Tunnel Lighting Design and Some Misplaced Applications in Turkey,www.emo.org.tr/ekler/b5cfc2cb39ac654_ek.pdf (Last access date: 02/05/2018).

[5] G. Parise, L. Martirano, and L. Parise, The energetic impact of the lighting system in the road tunnels. In Industrial & Commercial Power Systems Technical Conference (I&CPS) IEEE IEEE/IAS 51st, 1-7, (2015).

[6] International Commission on Illumination, Technical Report CIE 088:2004, Guide for the Lighting of Road Tunnels and Underpasses, 3-5, (2004).

[7] K. İzbek, Tunnel Lighting Technique (In Turkish Language) Ege University Printing Office, ISBN-ISSN: 9944595802, 118-144, (2006).

[8] International Commission on Illumination, Technical Report CIE 088:1990, Guide for the Lighting of Road Tunnels and Underpasses, 30-36, (1990).

[9] Thorn Lighting Holdings Ltd, Tunnel Lightning http://ww.thornlighting.com/download/TunnelINT. pdf, (Last access date: 02/05/2018).

[10] F. J. Nogueira, and L. A. Vitoi, Street lighting LED luminaries replacing high pressure sodium lamps: Study of case, In Industry Applications IEEE (INDUSCON), 1-8, (2014).

[11] S. Cattini, and L. Rovati, Low-cost imaging photometer and calibration method for road tunnel lighting. IEEE Transactions on Instrumentation and Measurement, 61(5), 1181-1192, (2012).

[12] Lighting Unit's, Lighting Technologies, http://www.lightinglab.fi/IEAAnnex45/guidebook/5_lighting%20technologies.pdf, 93-134, (Last access date: 02/05/2018).

[13] R. Dzhusupova, J.F.G. Cobben, and W.L. Kling, Zero energy tunnel: Renewable energy generation and reduction of energy consumption. In Universities Power Engineering Conference (UPEC), 47th IEEE International, 1-6, (2012).

[14] Tridonic, Lighting Control System, http://www.tridonic.com/ae/download/data_sheets/DS_smartDIM_SM_lp_en.pdf, (Last access date: 02/05/2018).

[15] SGS Lighting Solution, http://sgslight.com/led-panel-work-with-dali, (Last access date: 02/05/2018).

[16] M. Magno, T. Polonelli, L. Benini, and E. Popovici, A low cost, highly scalable wireless sensor network solution to achieve smart LED light control for green buildings, IEEE Sensors Journal, 15(5), 2963-2973, (2015).

[17] Trabzon Tenth District Directorate of Highways, Technical Documents, (2016).

[18] H. Zeng, J. Qiu, X. Shen, G. Dai, P. Liu, and S. Le, Fuzzy control of LED tunnel lighting and energy conservation, Tsinghua Science & Technology, 16(6), 576-582, (2011).

[19] D. Wang, H. Jiang, J. Ma, and X. Zheng, Dynamic Dimming Control Method Research on Tunnel LED Lighting Based on LED Controllability, In Remote Sensing, Environment and Transportation Engineering (RSETE), IEEE. 2nd International Conference, 1-4, (2012).

[20] H. Yi, L. Changbin, W. Aiguo, and F. Shouzhong, LED lighting control system in tunnel based on intelligent illumination curve, In Intelligent Computation Technology and Automation (ICICTA), IEEE. Fifth International Conference, 698-701, (2012).

Biography

Alkan AKSOY was born in, 1980 in Trabzon, Turkey. He received his B.Sc. and M.Sc. degree in Electrical & Electronics Engineering from Karadeniz Technical University (KTU) in Trabzon, Turkey, in 2003 and 2016 respectively. He is currently a Lecturer in Electricity and Energy Department of KTU Sürmene Abdullah Kanca Vocational School. He is also Ph.D. candidate at Atatürk University.

E-mail: alkanaksoy@hotmail.com

An Assessment of Energy Production Capacity of Amasra Town Using Artificial Neural Networks

Ünal Kaya[1*], Yüksel Oğuz[2], Ümit Şenol[3]

[1*]Kastamonu University, Cide Rıfat Ilgaz Vocational School, Department of Electronics &Automation, Kastamonu, 37600, Turkey
[2]Afyon Kocatepe University, Faculty of Technology, Department of Electricity & Electronics, Afyon, 03100, Turkey
[3]General Directorate of TEIAS, Department of Load Dispatch, Ankara, 06100, Turkey

ABSTRACT This study aimed to estimate the amount of power can be generated using wind turbines in accordance with the wind speed data obtained from Amasra town, using Artificial Neural Networks (ANN) method. In the training of artificial neural network, wind speeds ranging between 0 and 20 m/s were used as artificial neural network input while the production data from six wind turbines (Gamesa G97-2MW, Suzlon S.88-2100, Siemens SWT-2.3-113, N100-2.5 MW, E82-3 MW, V117-3.3 MW) were used as ANN outputs. Moreover, wind speed data collected from Amasra during 2016 was used in the test phase. Hence, the energy generation capacity of Amasra was analyzed with different wind turbines.

Keywords: Artificial Neural Networks, Wind Power, Energy Potential

1. INTRODUCTION

Energy is one of the most important aspects in economic and social development of nations. Need for electrical power has been increasing gradually in parallel with the technological advancements. Recently, producing energy from reliable resources in an efficient and cost-effective manner has become of great importance [1]. Today, most of the countries depend on fossil fuels such as coal, oil and natural gas to meet their energy demands. Considered to be one of the reasons behind global warming, the use of fossil fuels results also in air pollution, acid rains, ozone depletion, and deforestation [2]. With the depleting fossil fuel resources and due to the damages caused by the use of such resources, nations are now seeking the ways to utilize renewable energy resources. Nevertheless, it is only possible to meet the ever-increasing demand in energy using sustainable and clean energy resources, in other words, renewable energy resources [3].

Offering a great potential, renewable energy resources have recently found their place in the energy policies of nations and are becoming even more attractive investment options as the technology develops. Wind is one of the most important renewable energy resources which can compete with conventional energy resources thanks to the current technology and advancements in its use [4]. Wind power has been harvested since the ancient times through wind mills, and utilized in water pumps, sea and river shipping, and a number of mechanically powered devices. Today we have modern turbines designed to harvest wind power which are commonly exploited in many parts of the world [5]. Wind power offers various advantages including it is a clean and inexhaustible energy source, and it reduces the energy dependency of nations, its installation time is fast, and it's highly unlikely affected by the global energy market.

Since the 1990s, wind power technology has seen significant advancements and high-capacity wind farms have been built all around the globe. The total installed capacity of wind farms was 2.16 GW by the beginning of 1990s and it reached up to 13.5 GW by the end of 1990s, increasing approximately 6-fold. The increase in installed capacity persisted also in 2000s reaching up to 33.4 GW by the end of 2003, 74 GW by the end of 2006 and 487 GW by the end of 2016 as shown in Fig. 1 [6].
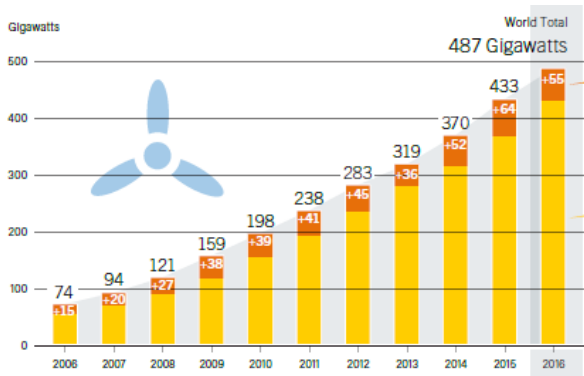
Fig. 1. The graph showing the installed wind power on Earth [6]

Turkey is a bridge between Europe and Asia, and it is surrounded by seas on its three sides. The coastal regions of Marmara, Aegean, and Eastern and Southeastern Anatolia offer a significant potential for wind energy with an average wind speeds between 4.5 to 10 m/sec. [7]. In Turkey, electricity generation based on wind energy started in 1998 with the first wind farm connected to the grid and the installed capacity and power production of wind farms has been increased significantly, especially after 2005. As of January, in 2017, the installed wind power capacity in Turkey has reached up to 6106 MW which corresponds to the 6.3% of the total installed power capacity of Turkey [8].
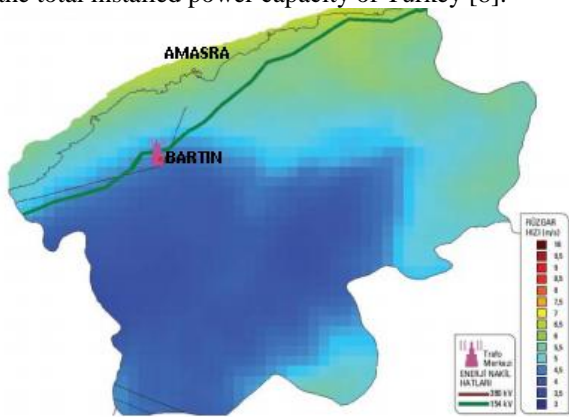

Fig. 2. A map of wind speed averages in Bartın

As shown in Fig. 2, Amasra is the district of Bartın with the highest wind potential. The reason behind the selection of Amasra in this study is that the wind speeds measured in this location reach up to 7 m/sec.

In this study, power production using wind energy was estimated by using ANN model in combination with a number of different wind turbine models. ANN was executed using Matlab software (version R2014A). The main purpose of this study was to define the wind energy potential of Amasra with minimal error using Artificial Neural Networks. Moreover, wind turbine models of Gamesa G97, Suzlon S.88, Siemens SWT2.3, Nordex N100, Enercon E82, Vestas V117 and the tower height of 90 m were selected as the ANN output data. These turbine models, output data of the ANN model, are commonly used in the industry offering significantly higher yields.

2. ARTIFICIAL NEURAL NETWORKS (ANN)

ANN is a computer system which is able to produce new information through learning, multiplexing, and exploration, just like human brain, and to perform superior skills without any kind of assistance [9]. As a result of advancement in computing algorithms and software industry, ANN modeling is now simpler and it offers convenient solutions to once hard-to-solve problems. In addition, ANN is widely used in engineering practices, especially in modeling complex problems. ANN, in short, is a set of artificial neurons developed upon inspiration of biological neurons. The most important features of ANN are its ability to model nonlinear systems, its structure with parallel distribution, error tolerance, ability to learn, generalize, and adaptability to different problems [10].

A basic ANN neuron has a much simpler structure when compared to a biological neuron. ANN model consists of an input layer, an output layer and a hidden layer. The hidden layer may consist of multiple layers and each layer contains neurons. Input layer includes a number of neurons equals to the number of variables while the output layer includes a number of neurons equals to the number of outputs. However, there are no rules dictating the number of neurons included in the hidden layer. Each neuron uses the output value of the neuron available in the previous layer as its input value. Neurons located in the interim layer and output layer process the signals they receive in accordance with a specific activation function and pass them to the next layer, if there is available. Activation functions are the functions shaping the output of ANN. An ANN model with an interim layer and sufficient amount of neurons in this layer is able to model any nonlinear function [11]. It is necessary to select the activation function corresponding to the type of the problem to be solved by ANN. The network must be required the applicable to attain the desired result in artificial neural networks. To realize this, weights with value suitable and accurate connections must be required. The network must learn the system's behavior or self-organize to meet these conditions [12].

Doğancı et al. (2016) conducted a study to estimate the wind power by measuring the wind power from several locations in Central and Western Black Sea Region. The study showed that estimates based on different parameters such as algorithm type, activation function, training function, number of layer, and number of neurons and actual measurements for Bafra, İnebolu, Zonguldak and Karabük were in agreement [13].

Kılıç & Arabacı (2016) estimated the wind speed values for the city of Burdur using ANN method. Calculations with the data obtained from Turkish Meteorological Institute showed that the ANN method is suitable methodology that can be used in similar studies [14].

Islak et al. have estimated the mechanical and physical properties of Cu-TiC composites produced by hot pressing technique with artificial neural networks (ANN) model. The output values have been selected as relative density, hardness, electrical conductivity, cross-

fracture strength, friction coefficient and wear rate while the input parameters have been selected as the amount of titanium carbide added copper matrix in the ANN model. As a result, the regression values were noted to be very close to the value of 1. This implies that the ANN model output is in well agreement with the real data [15].

Güleç et al. (2017) tried to estimate the wind power potential of the city of Kastamonu using two different models with several wind turbine data. The daily maximum wind speed data collected in 2015 for Kastamonu was acquired from General Directorate of Meteorology. As a result, maximum power values which can be produced per type of turbine were estimated. The estimates showed that Kastamonu offers a rather high wind potential [16].

Yiğit and his colleagues (2014) designed a web-based program to support the training of artificial neural network structures and the lesson contents. ANN model in order to test thanks to developed software and it is easier infer to understand the basics of YSA [17].

3. RESULTS AND DISCUSSIONS

In this study, the wind power production capacity of Amasra, a district of Bartın, was estimated using artificial neural networks with meteorological data. First, ANN model was trained using the responses of six different turbine models at varying wind speeds. Monthly average wind speed values measured in Amasra for 2016 were used as training input data.

Table 1. Monthly average wind speeds measured in Amasra in 2016

Months	Wind speed (m/s)
January	6.52
February	5.11
Arch	4.76
April	4.36
May	4.21
June	3.77
July	3.88
August	3.91
September	4.75
October	4.43
November	5.11
December	6.17

The production capacities of turbine types of Gamesa G97-2MW, Suzlon S.88-2100, Siemens SWT-2.3-113, N100-2.5 MW, E82-3 MW, V117-3.3 MW with respect to wind speed were used as training output data.
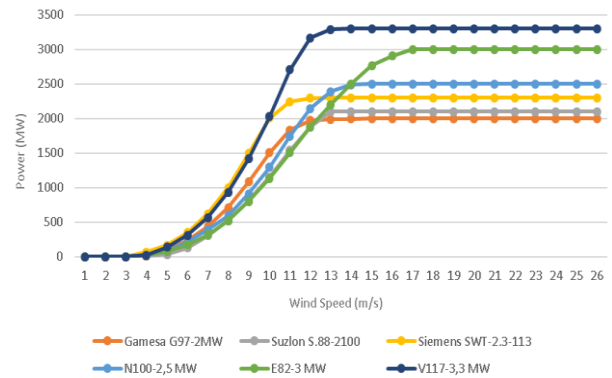

Fig. 3. The power generated by six turbines used in the ANN model with respect to the wind speed

Stopping criteria of "1,000" iterations, "0" error, gradient of 1e.-5 and number of "1,000" validation were used in the training process. Training reached at "1,000" iterations in 4 seconds and stopped. Dividend function, on the other hand, was divided in itself into two as train, validation and test in a randomized distribution of data in 70%, 15% and 15%, respectively. Mean squared error (mse) was used as the performance function. Fig. 4 shows the results of regression, validation, test data and training data. The model tends to memorize if the selected correction error gradient is high.
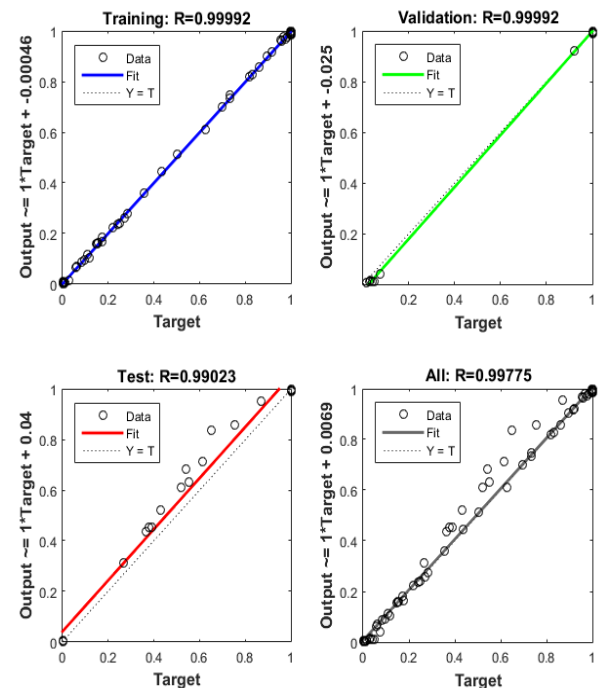
Fig. 4. Regression curves of the results of train, validation, test data and all data combined

Table 1 shows the data obtained from the Directorate of Meteorology for monthly average wind speed values measured at the city center of Amasra in 2016. Using the wind data for the city center of Amasra in the ANN model it is possible to obtain output power values corresponding to 6 turbines. These power values estimated are given in Table 2. Accordingly, it was found that Siemens SWT-2.3-113 is the most efficient turbine type.

Fig. 5. The amount of power obtained for six types of turbines may generate in Amasra

Table 2: The amount of power that can be generated by six different types of turbines in Amasra

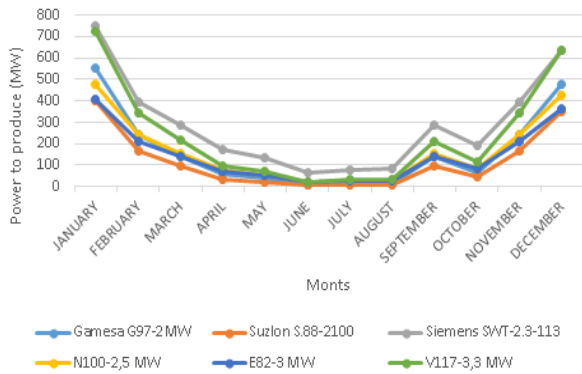| Months	Wind Turbines					
	Gamesa G97-2 MW	Suzlon S.88-2100	Siemens SWT-2.3-113	N100-2.5 MW	E82-3 MW	V117-3.3 MW
January	554.90	401.52	748.08	477.50	405.60	726.52
February	240.03	169.45	393.80	240.37	210.62	346.28
March	141.19	95.58	289.70	156.13	140.47	216.78
April	56.98	36.33	172.48	75.34	71.41	97.91
May	37.90	23.60	136.46	54.39	52.86	68.56
June	10.97	6.40	66.45	20.23	21.27	23.21
July	14.84	8.79	79.27	25.74	26.54	30.22
August	16.14	9.60	83.25	27.53	28.24	32.53
September	138.57	93.68	286.61	153.78	138.50	213.24
October	68.22	43.98	191.21	87.03	81.60	114.61
November	240.03	169.45	393.80	240.37	210.62	346.28
December	478.43	351.16	636.84	424.29	362.10	639.11

IV. CONCLUSION

The main purpose of this study was to reveal the wind energy potential of Amasra with minimal error using Artificial Neural Networks. The data obtained from Provincial Based Wind Energy Potential Atlas (Republic of Turkey Ministry of Energy and Natural Resources) shows that Amasra offers an important potential for wind [8, 18]. A closer look into the potential of Amasra comparing a number of turbines revealed that Siemens SWT-2.3-113 model turbine can generate attractive levels of energy in Amasra. The response of ANN model showed that Amasra is suitable for installation of turbines. These results are important especially in terms of the development of the city of Bartın and Western Black Sea Region.

References

[1] E. Yağcı, Comparison and error analysis of different methods used for wind speed extrapolation, M.Sc. Thesis, İstanbul University, Energy Science and Technology Department Energy Science and Technology Program, İstanbul. (2013).

[2] R. J. Wai, W. H. Wang, C. Y. Lin, High-performance stand-alone photovoltaic generation system, IEEE Transactions On Industrial Electronics, 55(1), 240-250, (2008).

[3] K. Azad, M. G. Rasul, R. Islam, I. R. Shishir, Analysis of wind energy prospect for power generation by three weibull distribution methods, Energy Procedia, 75, 722-727, (2015).

[4] U. Elibüyük, İ. Üçgül, A. K. Yakut, Wind power plant project to Suleyman Demirel University, Süleyman Demirel University, Journal of YEKARUM, 3(2), 22-32, (2016).

[5] A.V. Da Rosa, Fundamentals of renewable energy processes, 3rd ed., Amsterdam, Netherlands, Elsevier, (2013)

[6] REN21, Renewables 2017 Global Status Report, http://www.ren21.net/wp_content/uploads/2017/06/GSR2017_Full-Report.pdf, ISBN 978-3-9818107-6-9, (Accessed 2016).

[7] C. İlkiliç, İ. Türkbay, Determination and utilization of wind energy potential for Turkey. Renewable and Sustainable Energy Reviews, 14(8), 2202-2207, (2010).

[8] TUREB, Turkey wind energy statistics report Turkey wind energy association, http://www.tureb.com.tr, (Accessed 25.02.2017).

[9] E. Öztemel, Yapay sinir ağları, Papatya Yayıncılık, İstanbul, (2003)

[10] C. Hamzaçebi, Yapay sinir ağları: tahmin amaçlı kullanımı matlab ve neurosolution uygulamalı, Ekin Yayınevi, Bursa, (2011)

[11] L. Fausett, Fundamentals of neural networks: Architectures, Algorithms and Applications, Prentice Hall, New York, (1994)

[12] Ç. Elmas, Yapay Zeka Uygulamaları, Seçkin Yayıncılık, Ankara, (2011)

[13] Ö. Doğancı, M. Ertürk, A. Özsunar, A. Arcaklıoğlu, A study of the estimation of the wind energy in the central-western Black Sea region, Journal of Advanced Technology Sciences, 5(1), 153-163. (2016).

[14] B. Kılıç, E. Arabacı, Estimation of wind speed values in future of Burdur city using artificial neural networks (ANN), Dumlupınar University, Journal of Science and Technology of Dumlupınar University, 45-50, (2015).

[15] S. Islak, M, Akkaş, Ü, Kaya, H. Güleç, Estimation of mechanical and physical properties of Cu-Tic composites by artificial neural networks (ANN) Model, Technological Applied Sciences, 12, 122-129, (2017).

[16] H.G. Güleç, H. Demirel, Artificial neural network based prediction of intensity of insolation in the city of Kastamonu using meteorological data, Technological Applied Sciences, (2017).

[17] T. Yiğit, A. H. Işık, M. Bilen, Web based educational software for artificial neural networks, International Conference on Education in Mathematics, Science & Technology, May 16 – 18, 629-632, (2014).

[18] General directorate of renewable energy, http://www.eie.gov.tr/yekrepa/BARTIN-REPA.pdf (Accessed 08.03.2017).

Biographies

Ünal Kaya was born in 1986 in Fatih, İstanbul. After studying primary and high schools in İstanbul, he holds B.Sc. and M.Sc. degrees from Fırat University and was employed by Kastamonu University in 2013. Mr. Kaya specializes in artificial intelligence methods, energy and real-time control systems. Mr. Kaya is married with one child, currently employed in Cide Rıfat Ilgaz Vocational School.

E-mail: ukaya@gmail.com

Yüksel OĞUZ was born in Afyon, Turkey, in 1971. He received his B.Sc. degree from the Marmara University Technical Education Faculty, Department of Electrical Education, Istanbul, and the M.Sc. and Ph.D. degrees in Electrical Education from the Marmara University, Institute for Graduate Studies in Natural and Applied Sciences, in 2000 and 2007, respectively. He has been an assistant professor in the Electronical Engineering Department at Afyon Kocatepe University. He has worked mainly in control education, automatic control applications, electrical machines, power generation systems and control, renewable energy, and intelligent control.

E-mail: yukseloguz@aku.edu.tr

Umit Senol was born in 1989 in Sarikaya, Yozgat. After studying primary and high schools in Yozgat, he graduated from Dumlupinar University with a B.Sc. degree, and Bozok University with M.Sc. degrees. Mr. Senol specializes in renewable energy sources and artificial intelligence methods. Mr. Senol has been employed in Turkish Electricity Transmission Corporation since 2014.

E-mail: umitsenol66@gmail.com

Multilayered Implantable Antenna Design for Biotelemetry Communication

Onur Gürdoğan, Alp Eren Aydın, Sıddık Cumhur Başaran*

Department of Electrical and Electronics Engineering, Akdeniz University, Antalya, Turkey

ABSTRACT In this paper, a multilayered implantable antenna for MICS band biotelemetry applications is introduced. The proposed antenna has a fairly compact design with three layers. The primary radiator of the antenna consists of split-ring elements providing miniaturization. The antenna exhibits uniform radiation pattern for both *E* and *H*-plane and acceptable gain performance at desired frequency band. Analysis and design of the antenna was carried out using CST Microwave Studio and the results were validated by means of ANSYS HFSS simulator.

Keywords: Antenna design, Implantable, MICS band, Biotelemetry

Cite this article: O. Gürdoğan, A. E. Aydın, S. C. Başaran, Multilayered Implantable Antenna Design for Biotelemetry Communication, Turkish Journal of Electromechanics & Energy 3(1) 27-30 (2018).

1. INTRODUCTION

Recently, there is a growing research activity on short-range wireless biotelemetry applications in treating human diseases and monitoring various physiological parameters. Pacemaker communication, body temperature, respiratory rate, blood sugar, oxygen content of blood monitoring and endoscopy are just a few examples of the applications. Thanks to the biotelemetry, the physiological signals are wirelessly transceived between implantable medical devices and exterior equipment. In addition, for the communication between an implanted system and exterior monitoring or control equipment, wireless links are essential for the whole biotelemetry system. A typical biotelemetry system comprises a biosensor appropriate for the particular signals to be monitored, battery, a transmitter and an antenna. Among all the components necessary for implanted telemetry applications, the antenna plays a key role in obtaining robust communication network as well as in miniaturization of the whole device [2-5]. Besides, the difficulties in achievement of an optimum design by optimizing simultaneously the basic parameters such as its structure in compliance with the body physiology, electrically of dimensions, bandwidth, radiation efficiency and Specific Absorption Rate (SAR) values increase the significance and value of designing such an antenna at a higher level.

Communication Services (MICS, 402.0–405.0 MHz) is the most commonly used for the biotelemetry system [1]. The spectrum of 3 MHz allows for 10 channels (a bandwidth of 300 KHz each) to support simultaneous operation of multiple implantable medical devices in the same area, and to limit interference from the co-located Meteorological Aids Service band (401-406 MHz). Nevertheless, Industrial, Scientific and Medical (ISM, 2.4-2.84 GHz) band is also used for biomedical telemetry systems. Implant Communication Services is used for communication between implant and external unit. ISM band is used for sending a wake-up signal from external unit. For wake-up signal, the communication operates at certain intervals, so battery life can be improved. Also, more batteries can be inserted in the implant device with obtaining more miniaturized antenna.

In authors' earlier works, a split-ring (SR) [6] as well as a complementary split-ring [7] based novel implantable antenna designs were proposed. In current study, we employed a multilayer structure inspired by the antenna design reported in [8] in order to achieve a smaller antenna configuration as compared to the designs developed in [6, 7]. The radiating top layer of the antenna is composed of three concentric square SR elements as shown in Figure 1. The proposed antenna with novel configuration provides a single band performance at 400 MHz MICS band. The full-wave analysis of the proposed design was carried out using CST Microwave Studio, utilizing the time-domain finite-integration technique. Besides, Ansoft HFSS based simulation results was also introduced and presented to have cross-comparison for the return loss

characteristics of the proposed antenna. In this paper, the simulated return loss, radiation pattern and SAR values at the respective frequency band are presented.

2. ANTENNA DESIGN

The designed antenna has dimensions of 10×10×2.01 mm in three layer configuration. It is of outmost importance and desire to have minimum dimensions for the antenna when its implantation is taken into consideration. The frequency value that the antenna operates is the MICS (402-405 MHz) band allocated for biomedical applications. The proposed antenna consists of three layers. The bottom part of the substrate structure is used as the ground plane, and part there is a patch as the first radiation element on the top part. Above the second substrate is another second radiation element in the structure. Above all these layers, there is a top layer material. These structures, called superstrate as shown in Figure 1 (d), are made of the same material as the other two substrate structures. The purpose of their use is to gain a high directionality to the antennas and to allow them to radiate at a wide band gap [8]. The design has a short pin structure that connects the ground layer and the first radiation structure. The purpose of this short-circuiting pin is to reduce the antenna size by half, as well as to reduce the antenna's resonance frequency by half. Rogers RO3010 material was used as the substrate in the antenna design. The dielectric constant of Rogers RO3010 material is $\varepsilon_r = 10.2$. Three layers of RO3010 material were used in the design. In the design of the antenna, a slit is opened in the ground layer to reduce the resonance frequency in addition to make a sharp adjustment in resonance frequency values. The final dimensions of the antenna are recorded as follows (all in millimeters): $L=W=10$, $a = 0.3$, $a_1 = 1.5$, $a_2 = 1$, $L_1 = 8$, $L_2 = 5$, $L_3 = 3$, $W_1 = 5$, $W_2 = 8$, $W_3 = 5.5$, $l = 1.30$, $h = 12$, $h_1 = 0.67$, $h_2 = 5$. The layers of the designed antenna are shown in Figure 1. The size of the ground layer is 10×10 mm. The circular structure seen almost in the middle of the Figure 1 (a) indicates the location of the short-circuit pin. The other circle structure in the lower right part indicates the position of the coaxial feed structure. Above the ground layer, there is the first substrate structure with the first radiation structure. The substrate layer is 10×10 mm while the first layer of radiation on it is 8×8 mm in size. In Figure 1 (b), there is a meander line parasitic patch providing enhancement of antenna bandwidth. In the second layer of the antenna shown in Figure 1 (c), three concentric SR elements are used for primary radiators of the antenna. The substrate structure on the second patch layer is 10×10 mm in size. The size of the patch with SR structure is 8×7.5 mm. SR structures are preferred in this design because they reduce the resonance frequency. A square patch joint was made with the outermost ring physically touching the ring immediately inside, with a radius of 0.3 mm and allowing for precise frequency adjustments. These patches, especially used in fine frequency adjustments, help the antenna to radiate to the desired frequency. Changes can be made to the frequencies at which the antenna enters the resonance by changing its location. As shown in Figure 1, the transmission paths in this layer are 0.5 mm thinner than the transmission paths in the first layer. The reason for this is to increase the number of rings in the interior and reduce the spacing between them by bringing the rings together. Narrowing the paths between the rings allows us to obtain high capacitance values and also allows us to reduce the resonance frequency.
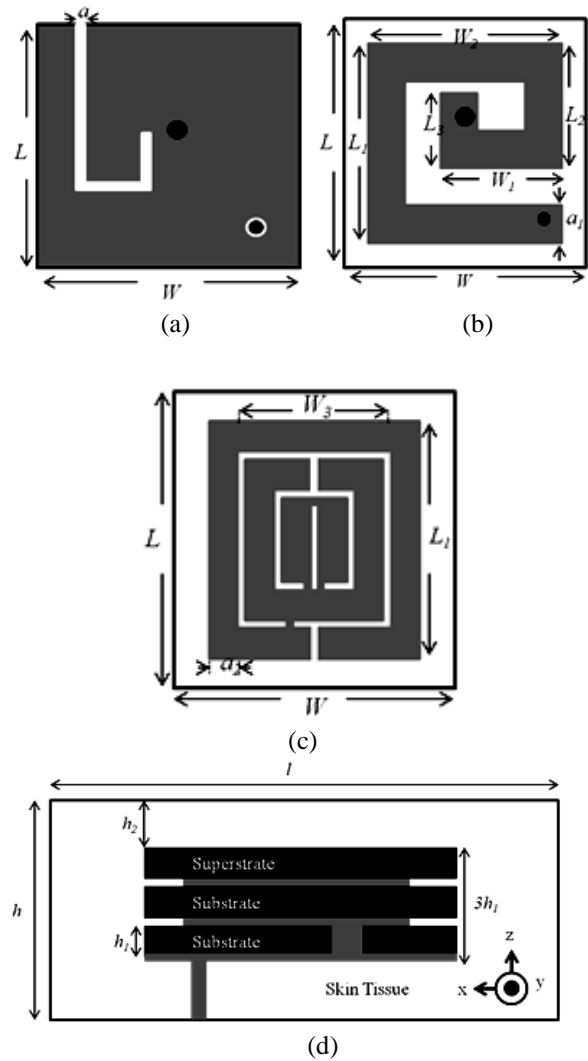

Fig. 1. Configuration of the proposed antenna with its design parameters; (a) Ground plane, (b) Lower radiation layer, (c) Upper radiation layer, (d) Side view of the antenna

3. EXPERIMENTAL RESULTS

In this study, we have mainly used the commercially available CST Microwave Studio during the design stage, due to its speed advantage. The High Frequency Structure Simulator (HFSS, a FEM based full-wave analysis tool with dissimilar modeling capabilities) was also employed to compare the results obtained from the CST. In particular, the truncation schemes differ in each simulator. As a result, some discrepancies in the HFSS and CST simulation results were observed. As it can be seen in Figure 2, the antenna provides a single band performance at frequency of 400 MHz with 40.44 MHz band width. Moreover, radiation patterns in the MICS band of the antenna are shown in Figure 3. As seen the antenna exhibits uniform radiation pattern in the both zx and zy-plane at the respective band.

Additionally, we simulated the proposed antenna in the skin tissue model to obtain 1-g averaged SAR values at respective frequency bands. For standard CST input power, maximum SAR values are obtain as 287.1 W/kg at 400 MHz as shown in Figure 4. Therefore, the delivered power of the antenna input must be arranged to satisfy SAR regulations (2 W/kg) of IEEE. For 402

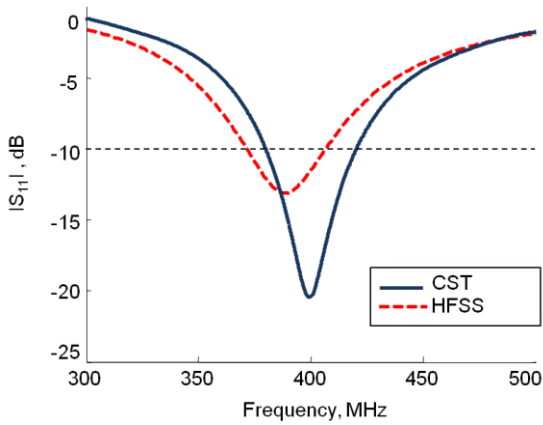MHz, maximum input power has to be lower than 5.57 mW.

Fig. 2. Comparison of return loss performance of the antenna (CST vs. HFSS softwares)
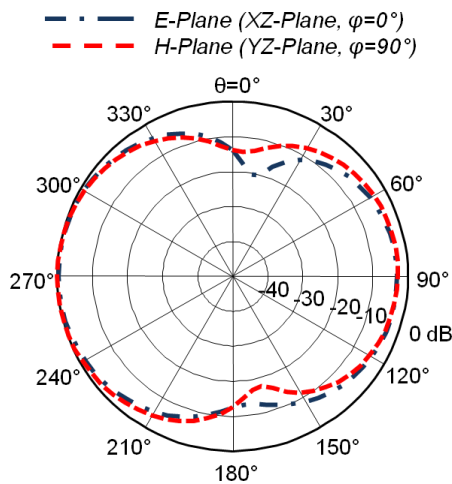

Fig. 3. Farfield realized radiation pattern *E*-plane and *H*-plane for the proposed antenna at 400 MHz
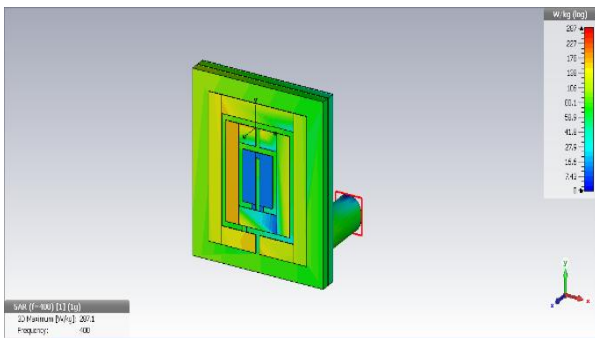

Fig. 4. SAR distribution in the skin tissue model for 400 MHz

4. CONCLUSION

We presented a novel multilayered implantable antenna for MICS band applications. In order to keep the antenna size small, a split-ring based radiator with a shorting pin is used. The antenna is excited by a coaxial probe feed and provides a single band operation about 400 MHz. The antenna exhibits nearly uniform radiation patterns and the SAR values of the antenna satisfy the standard safety guidelines in the band.

References

[1] "International Telecommunications Union Radio Communications (ITU-R), Radio Regulations, SA.1346, ITU, Geneva, Switzerland, (2016).

[2] A. Kiourti and K.S. Nikita, Miniature Scalp-Implantable Antennas for Telemetry in the MICS and ISM Bands: Design, Safety Considerations and Link Budget Analysis, IEEE Trans. Antennas Propag., 60(8), 3568–3575, (2012).

[3] A. Akbarpour, and S. Chamaani, Dual-band electrically coupled loop antenna for implant applications, IET Microw. Antennas Propag., 11(7), 1020-1023 (2017).

[4] L. Matekovits, Y. Su, and I. Peter, On the radiation mechanism of implanted antennas with large conformal ground plane, IET Microw. Antennas Propag, 11(12), 1765-1769, (2017).

[5] E. Uras, M.H.B. Ucar, and A. Sondas, A Miniature Implantable Microstrip Antenna Design for Dual-Band Biotelemetry Operations, in Proc. Computational Electromagnetics International Workshop (CEM), 58, İzmir, Turkey, (2015).

[6] Y. E. Yamaç, S. C. Başaran, A Compact Dual Band Implantable Antenna Based on Split-Ring Resonators with Meander Line Slots, 22nd International Conference on Applied Electromagnetics and Communications-ICECOM 2016, 1-3, Dubrovnik, Croatia, 19-21 September, (2016).

[7] M. Usluer, S. C. Başaran, Dual Band Implantable Antenna for Biomedical Applications, URSI Commission B International Symposium on Electromagnetic Theory (EMTS 2016), 530-531, Espoo, Finland, 13-18 August, (2016).

[8] K. Joshi, S. Saraswat, G. Gulati, V. Tiwari, Superstrate Layer in Patch Antenna – A Review, International Journal of Latest Trends in Engineering and Technology, 6(2), November, (2015).

Biographies

Onur Gürdoğan was born in Antalya, Turkey, in 1993. He received the B.S. degree from the Akdeniz University in 2017, specializing on microwave, microstrip structures and antenna subjects. After graduation, he worked for a company for a short time that provides industrial engineering services as a RF/Hardware design engineer. Currently, he is satellite control engineer in TURKSAT A.Ş. Ankara/Gölbaşı. He continues to research in the field of microstrip structures including antennas and filters.

E-mail: gurdogan.onur@hotmail.com

Alp Eren Aydın was born in Bursa, Turkey, in 1992. He received the B.S. degrees from the Akdeniz University and carry on M.S. degrees from Bursa Technical University all in Electrical-Electronics Engineering, in 2016, 2018, respectively. His research interests include numerical analysis reconfigurable, implantable antennas for biomedical applications, and finite elements methods in electromagnetics.

E-mail: alp_eren_aydin92@outlook.com

Sıddık Cumhur Başaran was born in Bayburt, Turkey, in 1975. He received the B.S., M.S. and Ph.D. degrees from the Kocaeli University, all in electronics and communication engineering, in 1996, 2000 and 2008, respectively. During 2011–2012, he was a visiting scholar at the Ohio State University, Electroscience Laboratory. He has been an Associate Professor in the Department of Electrical-Electronics Engineering, Akdeniz University, Antalya, Turkey since 2010. His research interests include numerical analysis and design of conformal and reconfigurable antennas, implantable antennas for biomedical applications, and finite elements methods in electromagnetics.

E- mail: cbasaran@akdeniz.edu.tr